Flow field based data processing for the oscillating conical bob interfacial shear rheometer

J. Tajuelo* and M. A. Rubio

Departamento de Física Fundamental,

Universidad Nacional de Educación a Distancia, UNED. 28040 Madrid. Spain

J. M. Pastor

Complex System Group, Technical University of Madrid (ETSIAAB). 28040 Madrid. Spain

(Dated: November 5, 2017)

Abstract

A rotational rheometer can be used as an interfacial shear rheometer by means of proper accessories that allow one to shear fluid-fluid interfaces in a controlled manner. One of the most used accessories, even commercially available, is based on a biconical bob geometry. However, recovering the correct values of the rheological variables is far from trivial. A strategy that has proved to be successful in other interfacial shear rheometers is to properly account for the interface and subphase drags by numerically finding the corresponding flow fields and, then, use an iterative scheme to recover the proper values of the complex Boussinesq number and, consequently, the dynamic surface moduli. Here we propose to use such a scheme for the biconical bob oscillatory rheometer. We compare our solution with different well known previous approximations, and discuss under which conditions those approximations may lead to errors in the data processing. We have tested the performance of our design and numerical framework on several interfacial systems, comparing the results to those obtained through a magnetic needle rheometer (ISR). We demonstrate that, even for relatively low values of the Boussinesq number, the numerical flow field solution here proposed allows one to precisely reproduce the results obtained by the ISR, while those approximations based on a linear velocity decay at the interface may introduce spurious effects on the calculation of the dynamic surface moduli.

* jtajuelo@bec.uned.es

I. INTRODUCTION

Interfacial rheology is the field of science that studies the mechanical properties of two-dimensional systems, formed on fluid-fluid interfaces, from the relationship between shear, dilatational, or compressional stresses and deformation. Shear deformations are particularly suited for this study because interfacial systems usually show a strong dependence of their properties on the concentration of surface active substances, and shear rheology is performed at constant area. Understanding the interfacial rheological behavior of complex materials and how to modify their response to shear stresses is relevant because the dynamic surface moduli of interfaces play a crucial role in the behavior of numerous systems, from, for instance, foams or emulsions [1–3] to enhanced oil recovery processes [4, 5].

The experimental characterization of the mechanical properties of interfacial systems faces an unavoidable challenge: the separation of the interface contribution to the experimentally measured physical quantities from all of the other possible contributions (subphase drag, inertia of probes in motion, etc.). Generally speaking, the interface and subphase contributions can be separated by solving the velocity profile at the fluid forming the subphase and at the interface. This is why several analysis of the flow field corresponding to different interfacial shear rheometers can be found in the literature. In a pioneering work, Reynaert *et al.* [6] proposed a numerical scheme to solve the Navier-Stokes equation with the Boussinesq-Scriven boundary condition [7] at the interface to find the flow fields for the case of the shear channel of the magnetic needle interfacial shear rheometer. They showed that non-linear velocity profiles at the interface do appear for low values of the Boussinesq number, Bo. Indeed, they demonstrated that the simple subtraction of the subphase contribution leads to errors in the calculation of the dynamic surface moduli, so that an appropriate processing of the experimental data requires the consideration of a more refined velocity profile.

The same idea was implemented to analyze the double wall ring geometry [8] obtaining similar conclusions: the coupling between the surface and the subphase can lead to a non-linear velocity profile at the interface that must be considered when the subphase contribution is not negligible with respect to the surface contribution. Moreover, they used the flow field solution together with an iterative procedure to find the correct value of Bo from the experimental raw data. A similar data processing scheme was successfully used

later for the magnetic needle interfacial shear rheometer [9].

Interfacial rheometers based on rotational rheometers with appropriate fixtures and data processing are instruments of choice as starting instruments in interfacial rheology laboratories. The versatility of using a conventional rotational rheometer, with slight modifications, as an interfacial rheometer has motivated the development of different designs over the last decades. Perhaps the first contribution in this field was the bicone geometry [10]. Later, du Noüy ring fixtures were used to implement more sensitive configurations in rotational interfacial rheometers [11]. More recently, the above-mentioned double wall ring (DWR) geometry was proposed as a two-dimensional equivalent of a double wall Couette setup [8]. Although rotational interfacial rheometers typically do not achieve the instrument resolution reached by modern magnetic probe interfacial rheometers [12, 13], they are the instrument of choice when hard samples are measured because they can impose much higher shear stresses. In comparison, the DWR geometry is, in principle, more sensitive than the bicone geometry due to its much lower inertia and contact area with the lower and upper phases. Nevertheless, the bicone geometry is still extensively used in different fields [14–16] and is commercially available from several manufacturers.

In this work we focus on the most usual hydrodynamical configuration of the bicone rheometer, that of a stationary cup containing the fluids and a biconical bob performing an oscillatory motion (OB -oscillatory bob- hereafter). There is a lack of an explicit solution for this hydrodynamic problem in the literature. Indeed, the experimental works using this configuration of the bicone geometry refer to theoretical models devised for other hydrodynamical conditions or approximations based on them.

For instance, Oh *et al.* [17] proposed an exact solution of the velocity profile of a viscometer consisting on a stationary bicone suspended by a torsion wire and a cup rotating with constant angular velocity (this rotating cup system will be labeled as RC -rotating cup- hereafter). Because the velocity distributions at the interface and the fluid phases are supposed to be independent of time, inertial effects are not considered in this model.

Later, Ray *et al.* [18] proposed an exact solution of the bicone geometry in a different configuration: the cup is forced to oscillate at the desired frequency, and the bicone, suspended by a torsion wire, performs an oscillatory motion as a consequence of the subphase and surface drags on it (this configuration, in which both, the bicone and the cup perform an oscillatory motion, will be labeled as OC-OB hereafter).

Concerning the currently most usual configuration, the OB system, Erni *et al.* [10] proposed an approximate solution of the velocity profile by adapting the model proposed by Oh *et al.* for the RC viscometer, assuming that the velocity field corresponds to the Oh *et al.* solution for the instantaneous values of the speed. However, the Oh *et al.* solution pertains to the constant angular velocity condition, so that this approximation should certainly fail at high frequency, particularly when the subphase viscosity is relatively low (water subphases for instance).

The main goal of our work is to provide an accurate scheme to process data from biconical rotational rheometers, which are still widely used in many laboratories. As we show in the manuscript, till now the processing of all of those data has been based in a theoretical model strictly valid only for the constant rotation of a cup, which is obviously not the commonly used geometry. The central point of the present paper is to propose, in the same spirit as in [6, 8, 9], a practical approach based in a numerical solution of the flow field equations to calculate the values of the rheological parameters from the raw amplitude ratio and relative phase measurements. Our scheme allows any rheologist to build up a bicone interfacial shear rheometer around any classical rotational rheometer at his/her disposal in the laboratory, and to setup a proper data processing scheme that will improve the resolution of the instrument and will yield a proper separation between elastic and viscous components of the response.

The formulation of the hydrodynamical problem allows for a very simple adaptation to different configurations (stationary, rotating or oscillating cups and/or bobs) by just changing the boundary conditions. Here we focus on the application of this scheme (numerically finding the flow field plus iterative computation of Bo) to the most widely used [14–16] OB configuration. In that purpose we, first, check the performance of this scheme against configurations with well known exact solutions. Second, we analyze under which conditions, the simple adaptation of the RC viscometer proposed by Oh *et al.* to the OB problem may lead to significant errors in the data processing. Third, we apply our model to process the experimental raw data obtained from a conical bob geometry setup on a conventional rotational rheometer. Finally we crosscheck the validity of this model by performing experiments on interfaces with well known rheological behavior (thin films made of silicone oil) and on fatty acid Langmuir monolayers, comparing the results with those obtained by means of a different interfacial rheology technique (magnetic needle shear rheometer).

For the sake of clarity we have restricted the present study to air-liquid interfaces so that only the lower cone has to be taken into account. The extension of the analysis here reported to the two liquids case is, conceptually, straightforward, but it requires to include the effects of the hydrodynamic boundary conditions at the interface of the upper liquid with the upper cone and the bicone shaft, and at the upper liquid top surface.

II. MATERIALS AND METHODS

A. Experimental setup

The schematic of the device is shown in Fig. 1. The single-cone bob (1) was precision machined in aluminum, with a cone angle $\alpha = 5^\circ$ and radius $R_1 = 34\,\mathrm{mm}$. A very simple non optimized demonstration sample holder was machined in a single delrin block giving a cup (7), with radius $R = 40\,\mathrm{mm}$, and height $h = 22\,\mathrm{mm}$. The cylindrical Delrin cup is connected by means of a 4 mm wide and 6 mm deep channel (5) to a $7 \times 11 \times 0.6\,\mathrm{cm}$ Langmuir trough. The mobile Delrin barrier (4) is controlled by a linear stage (8) (TRA25CC, Newport) with a precision better than $1\,\mu\mathrm{m}$, so that the interface can be compressed and expanded. The surface pressure is measured at the Langmuir trough by means of a precision balance (3) (NIMA PS-4) with a paper Wilhelmy piece. The resolution in the surface pressure measurements is $\pm 0.05\,\mathrm{mN/m}$.

The conical bob is mounted on a conventional rotational rheometer (C-VOR, Bohlin Instruments). All of the measurements were performed in the stress controlled mode taking care that the stress amplitude was low enough to guarantee that the strain does not exceed the appropriate limit for each experiment. The bottom part of the Delrin cup was kept in good thermal contact with a stainless steel piece (2) having an inside fluid circulation coil (6) whose flow was driven by a Polyscience P-9010 thermostatic bath that provides a temperature stability of $\pm 0.01^\circ\mathrm{C}$.

A key parameter in the forthcoming analysis is the rotor+bob moment of inertia about the rotation axis. This parameter has been precisely measured performing frequency sweeps at fixed stress amplitude and fitting the angular displacement amplitude to the theoretical prediction (see supplementary material for details). The rotor+bob moment of inertia measured was $I = (2.42 \pm 0.02) \times 10^{-5}\,\mathrm{kg \cdot m^2}$.

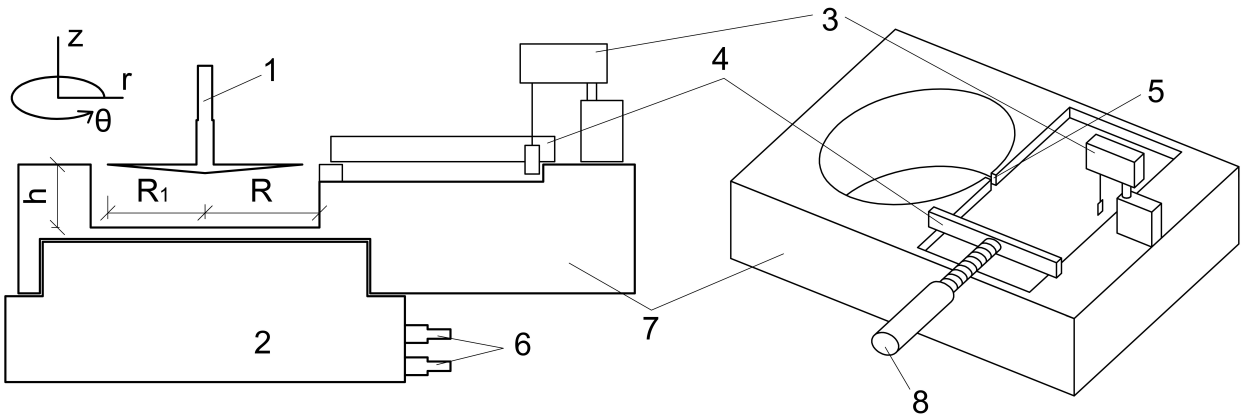

FIG. 1: Schematics of the conical bob and the measurement cell, comprising the following elements: (1) Aluminum conical bob, (2) Stainless steel cylinder with internal water circulation (Bohlin C-VOR), (3) Surface pressure sensor, (4) Delrin barrier, (5) Channel connecting the Langmuir trough and the cylindrical cup, (6) Thermostatic bath I/O, (7) Delrin measurement cell, and (8) Linear stage controlling the barrier displacement.

From the rheometer control software, provided by the manufacturer, we obtain the raw torque and angular position data. According to the technical datasheet of the rheometer, the nominal torque and position resolutions are $\Delta T = 1\mathrm{nN}\cdot\mathrm{m}$ and $\Delta\theta = 0.9\,\mu\mathrm{rad}$, respectively. Hence, in order to make precise stress controlled measurements with, let us say, less than 5% error in the selected torque, the minimal torque value that can be used is $T_{\min} = 20\mathrm{nN}\cdot\mathrm{m}$.

In the conical bob experiments, a continuous oscillatory motion is performed for a time lapse spanning six periods of the forcing frequency. The standard rheometer control software yields the raw torque and displacement data, the torque-displacement amplitude ratio, T_0/θ_0, and the phase lag, δ.

The experimental results obtained with the conical bob in the rotational rheometer have been cross-checked by comparing them with measurements on identical systems performed with a magnetic tweezers driven interfacial shear rheometer (ISR) [12]. Typically, we have used two different probes for the ISR: a conventional needle (KSV-NIMA, ISR38) with length $L_n = 38.3\,\mathrm{mm}$, mass $m_n = 15.8\,\mathrm{mg}$, and external diameter $d_n = 0.4\,\mathrm{mm}$, and a microwire probe [19] with length $L_{\mathrm{MW}} = 8.5\,\mathrm{mm}$, mass $m_{\mathrm{MW}} = 1.9\times10^{-2}\,\mathrm{mg}$, and external diameter $d_{\mathrm{MW}} = 24.6\,\mu\mathrm{m}$. The shear channel used in these experiments was 2 cm wide. The data processing for the calculation of the dynamical surface moduli has been fully described elsewhere [12].

Regarding the experiments on fatty acid monolayers, in both rheometers, they were performed under continuous compression at a constant rate of $0.2\,\mathrm{cm}^2/\mathrm{s}$ for the ISR, and $0.03\,\mathrm{cm}^2/\mathrm{s}$ for the conical bob rheometer. All of the oscillatory measurements were made at a constant frequency $f = \omega/(2\pi) = 0.5\,\mathrm{Hz}$. In both rheometers the amplitude of the probe oscillation (the magnetic needle or the conical bob) was adjusted in every experiment on fatty acid monolayers in order to keep the strain below 1%.

B. Test fluids

All of the experiments were carried out on air-water interfaces. The subphase was always formed by Milli-Q quality water obtained from a Millipore DirectQ3 system. In order to study the validity of the proposed analysis, we have experimentally studied purely viscous interfaces made of silicone oil thin films, and viscoelastic interfaces made of fatty acid Langmuir monolayers.

Purely viscous interfaces were prepared by spreading thin films of silicone oil (Fluka DC200, $\eta_1 = 33\,\mathrm{Pa}\cdot\mathrm{s}$ and $\eta_2 = 1\,\mathrm{Pa}\cdot\mathrm{s}$ at 25°C). The rheological experiments were performed after waiting for two hours, so that it is assumed that the silicone oil film was homogeneous in depth, ϵ. Being $\epsilon = V/A$, where A is the area of the free air-water interface, and V is the volume of silicone oil spread on the interface, the expected surface viscosity of the film is then given by $\eta_s = \eta\epsilon$ [9].

For reasons that will be discussed in the Section III C 2, we have chosen to measure viscoelastic interfaces formed by Langmuir monolayers of two different fatty acids: lignoceric acid (C24, Sigma Aldrich), and pentadecanoic acid (C15, Sigma Aldrich). The monolayers were formed by spreading a solution of the fatty acid in chloroform (Sigma-Aldrich CHROMASOLV) onto the air-water interface, and waiting for 25 min for chloroform evaporation and stabilization of surface pressure and temperature. The concentration of the fatty acid in chloroform solution was 1g/L for those experiments performed in the ISR, and $0.1\,\mathrm{g/L}$ for those experiments performed in the conical bob rheometer. The measurements were performed at the L2 phase of the C24 fatty acid, and the L2 and LS phases of the C15 fatty acid at a temperature of 25°C [20].

C. Hydrodynamical model for the oscillating conical bob problem

Following Reynaert *et al.* [6] we want to build a simple hydrodynamic model that will incorporate a description of the flow at the subphase, and, more importantly, the coupling between subphase and interfacial flow fields. The approximations here chosen are as follows:

a) The velocity fields at, both, the subphase and the interface are axisymmetric and horizontal. This means that the velocity fields can be represented, in cylindrical coordinates, by just azimuthal velocities that are functions independent of the azimuthal angle, θ, so that the problem can be formulated as a two-dimensional problem in the plane (r, z). More complex and accurate non horizontal representations of the velocity field at the subphase can be devised (see for instance the analysis in [21] for the knife edge viscometer). However, for the range of dynamic moduli measurable with the conical bob geometry and the small typical strains used in oscillatory measurements, these secondary flows should be hardly relevant, and would imply a much higher computational cost. We assume that the azimuthal velocity is low enough to neglect the occurrence of flow instabilities, since the bicone performs very small amplitude angular oscillations at frequencies below 10 Hz. Values of the Reynolds number will be given later in connection with the discussion of the experimental measurements.

b) The interface is horizontal.

c) The conical bob can be represented as a null thickness disk. In the oscillatory case, this approximation is valid provided that $h - \tan(\alpha)R_1 \gg \ell_\omega$, where ℓ_ω is the viscous length scale corresponding to the subphase, $\ell_\omega = \sqrt{\eta/(\rho\omega)}$ [22]. For a water subphase ($\eta = 1\,\mathrm{mPa}\cdot\mathrm{s}$) and the typical frequencies (0.05-5 Hz), this condition is satisfied (see supplementary material for details). In other words, because the length scale in which the subphase velocity decays is negligible with respect to the distance from any point of the cone surface to the bottom of the measurement cell, the velocity profile along any vertical axis for the conical bob is well approximated by the profile corresponding to a null thickness disk. In the constant rotation case, the relevant length scale is h and the approximation is valid provided that $\tan(\alpha)R_1 \ll h$.

In Fig. 1 we represent the geometrical parameters and the reference frame used in this study. Within the above mentioned approximations, the velocity of a fluid element, loca-

ted in the position (r, θ, z) in cylindrical coordinates, would be represented by a function $v_\theta(r, z, t)$. Then, the corresponding expression of the Navier-Stokes equations in cylindrical coordinates is

$$\frac{\partial v_\theta}{\partial t} = \frac{\eta}{\rho}\left(\frac{\partial^2 v_\theta}{\partial r^2} + \frac{\partial^2 v_\theta}{\partial z^2} + \frac{1}{r}\frac{\partial v_\theta}{\partial r} - \frac{v_\theta}{r^2}\right), \tag{1}$$

where η is the viscosity of the subphase fluid, and ρ is its density.

Let us consider that the disk is forced to perform an oscillatory displacement with angular amplitude θ_0 and angular frequency ω, i.e., $\theta(t) = \theta_0\, e^{i\omega t}$. The azimuthal velocity at the disk edge will then be $v_{\theta,d}(t) = i\, R_1 \omega\, \theta_0\, e^{i\omega t}$. Following Ref. [6], once the transients have decayed, we can represent the azimuthal velocity of any fluid element as proportional to the azimuthal velocity at the disk edge,

$$v_\theta(r, z, t) = g^*(r, z) v_{\theta,d}(t) = i\, R_1 \omega\, g^*(r, z) \theta_0 e^{i\omega t}, \tag{2}$$

where $g^*(r, z)$ is a complex function whose real and imaginary parts represent the components of the velocity of the fluid element in phase and out of phase with that of the disk, respectively. From the substitution of Eq. 2 in Eq. 1, the equation governing $g^*(r, z)$ is

$$i\,\omega\, g^*(r, z) = \frac{\eta}{\rho}\left(\frac{\partial^2 g^*(r, z)}{\partial r^2} + \frac{\partial^2 g^*(r, z)}{\partial z^2} + \frac{1}{r}\frac{\partial g^*(r, z)}{\partial r} - \frac{g^*(r, z)}{r^2}\right). \tag{3}$$

This equation can be written in non−dimensional form as

$$i\, Re\, g^*(\bar{r}, \bar{z}) = \frac{\partial^2 g^*(\bar{r}, \bar{z})}{\partial \bar{r}^2} + \frac{\partial^2 g^*(\bar{r}, \bar{z})}{\partial \bar{z}^2} + \frac{1}{\bar{r}}\frac{\partial g^*(\bar{r}, \bar{z})}{\partial \bar{r}} - \frac{g^*(\bar{r}, \bar{z})}{\bar{r}^2}, \tag{4}$$

where the symbols with overbars represent spatial variables that have been normalized by taking

$$\begin{aligned} \bar{r} &= \frac{r}{R} \text{ and} \\ \bar{z} &= \frac{z}{R}, \end{aligned} \tag{5}$$

and the Reynolds number has been defined as

$$Re = \frac{\rho \omega R^2}{\eta}. \tag{6}$$

The boundary conditions are no slip at the cup walls and bottom, zero velocity along the z axis, and no slip at the disk surface. These conditions can be represented in terms of the

function g^* as

$$g^*(\bar{r},0) = g^*(1,\bar{z}) = 0,$$
$$g^*(0,\bar{z}) = 0, \text{ and}$$
$$g^*(\bar{r} \leq \bar{R}_1, \bar{h}) = \frac{\bar{r}}{\bar{R}_1}. \tag{7}$$

The boundary condition at the air-water interface, i. e., for $\bar{R}_1 < \bar{r} < 1$ and $\bar{z} = \bar{h}$, is given by the Boussinesq-Scriven condition [7], which depends on the complex surface viscosity of the interface, $\eta_s^* = \eta_s' - i\eta_s''$. In cylindrical coordinates, this condition takes the form

$$\frac{\partial g^*}{\partial \bar{z}} = Bo^* \frac{\partial}{\partial \bar{r}} \left(\frac{1}{\bar{r}} \frac{\partial}{\partial \bar{r}} \left(\bar{r}\, g^* \right) \right) \text{, at } \bar{R}_1 < \bar{r} < 1,\ \bar{z} = \bar{h}, \tag{8}$$

where we have used the complex Boussinesq number, Bo^*, defined as [10, 18]

$$Bo^* = \frac{\eta_s' - i\eta_s''}{R\eta}. \tag{9}$$

We have solved Eq. 4 with the above mentioned boundary conditions by means of a second order forward and backward finite differences method within Mathematica (WolframAlpha). Given the symmetry of the problem, it suffices to solve Eq. 4 in the rectangle defined by $0 \leq \bar{r} \leq 1$ and $0 \leq \bar{z} \leq \bar{h}$. We performed thorough tests of the convergence and precision of the method depending on the spatial resolution chosen. The difference between the total torque calculated through the resolution of the flow field by using a mesh with 100 by 100 nodes in the $(\bar{r}, \bar{z})$ plane, and a mesh with 150 by 100 nodes in the $(\bar{r}, \bar{z})$ plane, is less than 0.1%. For the study here reported we used a mesh with 200 by 100 nodes in the $(\bar{r}, \bar{z})$ plane, which proved to be, both, highly precise and reasonably fast.

To illustrate the results of this model, we show in Figs. 2a and 2b the azimuthal velocity profile at the interface, $g^*(\bar{R}_1 \leq \bar{r} \leq 1, \bar{z} = \bar{h})$, for different values of ω and Bo^*. Filled symbols represent the real part of g^*, Re$[g^*]$, which is proportional to the component of the azimuthal interfacial velocity that is in phase with the azimuthal velocity of the disk. Open symbols represent the imaginary part of g^*, Im$[g^*]$, proportional to the component of the azimuthal interfacial velocity that is out of phase with the azimuthal velocity of the disk. Re$[g^*]$ is linear and Im$[g^*]$ is negligible for relatively high Boussinesq number and low frequency. However, as the Boussinesq number is decreased (Fig. 2a), or the frequency increased (Fig. 2b), Re$[g^*]$ decays in the vicinity of the disk edge, while Im$[g^*]$ becomes comparable in amplitude to Re$[g^*]$.

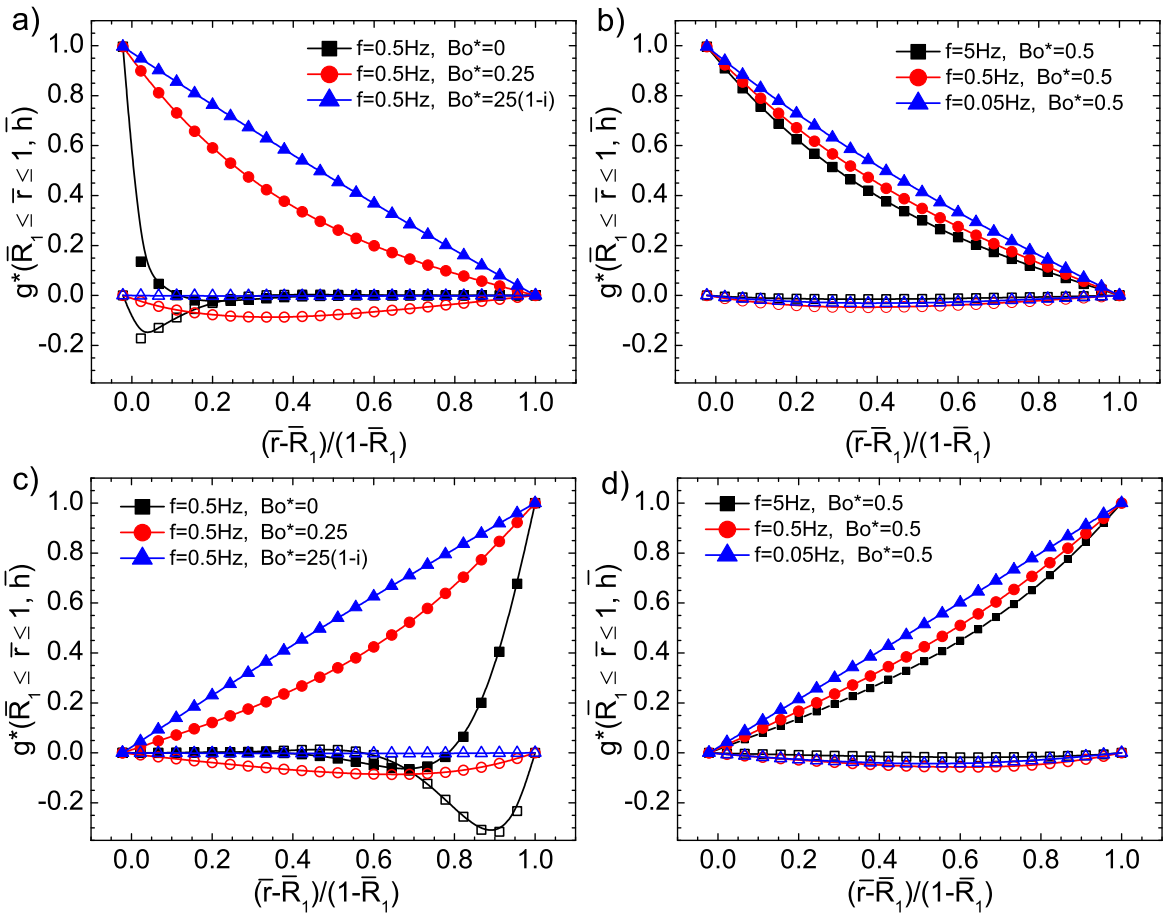

FIG. 2: Velocity profile at the interface for the geometrical parameters described in the Section II A, and calculated for different frequency (right) and Bo^* (left) values. Filled and open symbols correspond to the real and imaginary parts of g^*, respectively. a) and b) Oscillating conical bob and stationary cup system. c) and d) Oscillating cup and stationary conical bob system.

One interesting consequence when $\mathrm{Re}[g^*]$ not linear, is that $\partial \mathrm{Re}[g^*]/\partial \bar{r}$ at $\bar{r} = \bar{R}_1$ is higher in absolute value than the corresponding value for the linear profile. In consequence, the surface dynamic moduli calculated from the experimental data of torque and angular displacement assuming a linear velocity profile for v_θ at the interface would be overestimated. This phenomena will be analyzed in detail in the Section III B 2.

In Figs. 2c and 2d we plot the velocity profile at the interface for a different set of boundary conditions, namely, those corresponding to the stationary conical bob - oscillating cup configuration (OC hereafter). Full details of this calculation and its motivation will be

given in the Section III A 2. At this point, our purpose is to highlight that, for this system, the gradient of the azimuthal velocity at the interface is also higher at the mobile element (the cup in this case), and, more importantly, the radial component of the gradient of the velocity at $\bar{r} = 1$ and $\bar{r} = \bar{R}_1$ do not equal those corresponding to the OB system shown in Figs. 2a and 2b (this can be clearly seen in the curves corresponding to $Bo^* = 0$). In consequence, the drag on the conical bob and the cup in the OC configuration are necessarily different from those corresponding to the OB system.

Fig. 2 qualitatively shows the dependence of ℓ_ω^s [22], the size of the interfacial region necessary to bleed the conical bob (or cup) momentum into the bulk, on frequency and η_s^*. The velocity profile at the interface approaches a linear dependence on $\bar{r}$ as f decreases or η_s^* increases. Following Fitzgibbon *et al.* [22], we can define $\bar{\ell}_\omega^s$ as

$$\bar{\ell}_\omega^s = \frac{\ell_\omega^s}{R} = \frac{\ell_\omega \left|Bo_\omega^*\right|^{1/2}}{R} = \sqrt{\frac{\ell_\omega \left|Bo^*\right|}{R}} = \frac{1}{R}\sqrt{\frac{|\eta_s^*|}{\sqrt{\eta\rho\omega}}}, \tag{10}$$

where ℓ_ω is the viscous length scale defined previously, and Bo_ω^* is a frequency dependent Boussinesq number that uses ℓ_ω instead of R as length scale,

$$Bo_\omega^* = \frac{\eta_s' - i\eta_s''}{\eta\ell_\omega} = Bo^*\frac{R}{\ell_\omega} = \frac{Bo^*}{\bar{\ell}_\omega}. \tag{11}$$

Fig. 3 represents $\bar{\ell}_\omega$ versus $|Bo^*|$ for three different frequencies, $f = 0.05\,\mathrm{Hz}$, $f = 0.5\,\mathrm{Hz}$, and $f = 5\,\mathrm{Hz}$. The horizontal dotted line represents the width of the free interface given by the distance between the conical bob edge and the cup wall, $1 - \bar{R}_1$. The velocity profile at the interface is well represented by a linear dependence on $\bar{r}$ when $\bar{\ell}_\omega^s \gg 1 - \bar{R}_1$, being $1 - \bar{R}_1$ the characteristic length scale in these cases. On the contrary, the velocity decays in the vicinity of the mobile element when $\bar{\ell}_\omega^s \ll 1 - \bar{R}_1$, being $\bar{\ell}_\omega^s$ the characteristic distance at which the interfacial momentum is attenuated. We will return to the question of the characteristic length scale when discussing the differences between the OB, OC, and OC−OB configurations.

D. Data processing

Once the flow field is obtained through the numerical solution for $g^*(r, z)$ one can readily calculate, as will be shown in this Section, the subphase and surface drags on the conical bob and the cup in a single step, properly accounting for the possible existence of an out

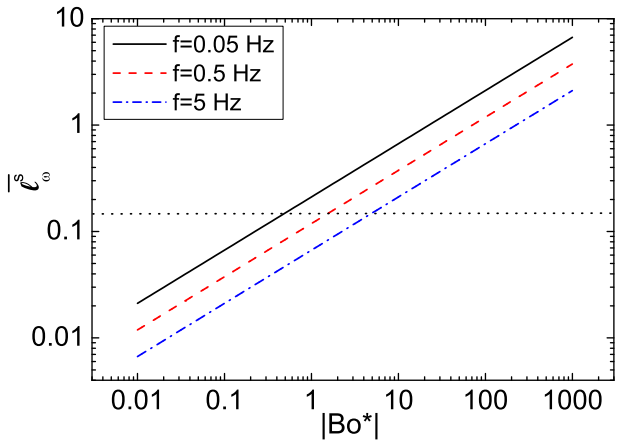

FIG. 3: Characteristic length at which the interface momentum is attenuated, $\bar{\ell}^s_\omega$, versus $|Bo^*|$, for three different frequencies, $f = 0.05\,\mathrm{Hz}$, $f = 0.5\,\mathrm{Hz}$, and $f = 5\,\mathrm{Hz}$. The horizontal dotted line represents the value $1 - \bar{R}_1 = 0.15$.

of phase component of v_θ and its non linearity. In addition, both the differential equation 4 and the boundary conditions given by Eqs. 7 can be easily adapted to obtain the flow field corresponding to different interfacial viscometric or rheometric systems, such as the stationary bicone-rotating cup (RC) viscometer [17], the oscillating cup and bicone rheometer (OB-OC) [18, 23], and the stationary cup and rotating bicone (RB hereafter) viscometer [10]. In the Sections III A 1 and III A 2 we will compare the flow field solutions here obtained with other previously reported for some of these systems, and discuss the performance of the different designs.

The rotational rheometer measures with good precision the torque imposed on the rotor+conical bob ensemble and its angular displacement, which can be represented as

$$\begin{aligned} \theta^*(t) &= \theta_0 e^{i\omega t}, \\ T^*(t) &= T_0 e^{i\omega t - \delta} = T_0^* e^{i\omega t}. \end{aligned} \tag{12}$$

From the relationship between the torque and the angular displacement, we can define the amplitude ratio and phase lag as

$$\begin{aligned} AR^* &= \frac{T_0^*}{\theta_0}, \\ \delta &= \arg\left(AR^*\right). \end{aligned} \tag{13}$$

The amplitude ratio and the phase lag are related to the interfacial dynamic moduli through

the torque balance equation

$$T^*(t) + T^*_{\rm sub}(t) + T^*_{\rm surf}(t) = I\frac{\partial^2\theta(t)}{\partial t^2}, \tag{14}$$

where $T^*_{\rm sub}$ and $T^*_{\rm surf}$ are, respectively, the subphase and surface drag terms. In principle, one might include a friction term proportional to $\partial\theta(t)/\partial t$ on the left hand side of Eq. 14 that would represent an eventual frictional torque appearing at the rotor air bearing of the rheometer. However, in the case of the rotational rheometer here used, careful checks, made by fitting the experimental rotor response to the application of a constant torque with finite initial angular velocity to the theoretical expression, show that this frictional torque on the rotor air bearing is always negligible when compared with the other terms in Eq. 14 (see supplementary material for details).

The subphase and surface drags can be calculated from the gradient of the azimuthal velocity on the conical bob lower surface and edge, respectively, as

$$\begin{aligned} T^*_{\rm sub} &= -\int_0^{R_1} \eta 2\pi r^2 \left(\frac{\partial v_\theta}{\partial z}\right)\bigg|_{z=h} dr \\ &= -i\omega 2\pi R_1 \eta\theta_0 e^{i\omega t}\int_0^{R_1} r^2 \left(\frac{\partial g^*}{\partial z}\right)\bigg|_{z=h} dr \text{ and} \\ T^*_{\rm surf} &= \eta^*_s 2\pi R_1^2 \left(\frac{\partial v_\theta}{\partial r} - \frac{v_\theta}{r}\right)\bigg|_{r=R_1,\, z=h} \\ &= i\omega 2\pi R_1^2 R\, Bo^* \eta\theta_0 e^{i\omega t}\left(R_1 \left(\frac{\partial g^*}{\partial r}\right)\bigg|_{r=R_1,\, z=h} - 1\right). \end{aligned} \tag{15}$$

The drags can be written in non−dimensional form as

$$\begin{aligned} \bar{T}^*_{\rm sub} &= -\bar{R}_1 \int_0^{\bar{R}_1} \bar{r}^2 \left(\frac{\partial g^*}{\partial \bar{z}}\right)\bigg|_{\bar{z}=\bar{h}} d\bar{r} \text{ and} \\ \bar{T}^*_{\rm surf} &= \bar{R}_1^2 \left(\bar{R}_1 \left(\frac{\partial g^*}{\partial \bar{r}}\right)\bigg|_{\bar{r}=\bar{R}_1,\bar{z}=\bar{h}} - 1\right), \end{aligned} \tag{16}$$

where the torque has been normalized as

$$\bar{T}^* = \frac{T^*}{i\omega 2\pi\theta_0 e^{i\omega t} R^3 \eta}. \tag{17}$$

Taking into account Eqs. 2, 14, and 15, the amplitude ratio, the azimuthal velocity amplitude function g^*, and the complex Boussinesq number, Bo^*, are related by the following expression

$$AR^* = i\omega 2\pi R_1\eta\left[\int_0^{R_1} r^2 \left(\frac{\partial g^*}{\partial z}\right)\bigg|_{z=h} dr - R_1 R\, Bo^*\left(R_1\left(\frac{\partial g^*}{\partial r}\right)\bigg|_{r=R_1,\, z=h} - 1\right)\right] - I\omega^2. \tag{18}$$

Observe that g^* depends on Bo^* in a non trivial way, so that this is an implicit equation in Bo^* and, consequently, cannot be solved directly. Instead, we build up a numerical iterative procedure similar to that proposed by Verwijlen *et al.* [9] for the magnetic needle interfacial shear rheometer, and successfully used later in [12, 19]. We start from the experimentally measured amplitude ratio, $AR^*_{\rm exp}$, and a suitable initial value of the complex Boussinesq number, $Bo^{*\{i=1\}}$. Solving the hydrodynamic equations for the flow field with $Bo^{*\{i=1\}}$ allows us to calculate the subphase and surface drag torques and to obtain the corresponding amplitude ratio from Eq. 18, $AR^*_{\rm calc}$. Then, we obtain a new corrected value for Bo^*, and we repeat the whole process with the newly obtained complex Boussinesq number in an iterative way, i.e.,

$$Bo^{*\{i+1\}} = \frac{AR^*_{\rm exp}}{AR^{*\{i\}}_{\rm calc}} Bo^{*\{i\}}. \tag{19}$$

This procedure is repeated until convergence is obtained. Throughout the rest of the paper, the convergence criterion employed is that $AR^*_{\rm calc}$ and $AR^*_{\rm exp}$ coincide within 0.1%. Then, the dynamic surface moduli, G'_s and G''_s are obtained from the definition of the complex Boussinesq number

$$G''_s - iG'_s = \omega R \eta Bo^*, \tag{20}$$

where the complex dynamic surface moduli and the complex surface viscosity are related by

$$G^*_s = i\omega\eta^*_s. \tag{21}$$

Typically, the number of iterations required to reach convergence depends on the relative importance of the surface drag when compared to the subphase drag and the rotor inertia. The higher the surface drag, the lower number of iterations is needed. For the reported experiments, the number of iterations varies from 10 to 150.

III. RESULTS AND DISCUSSION

The goal of this report is to illustrate the performance of the application of the above described computational scheme to the nowadays more popular configuration of rotational bicone rheometers, namely the one with oscillating bicone and stationary cup. With that in mind, we will start by discussing the application to some other benchmark configurations taking advantage of the scheme versatility.

A. Benchmarking the numerical scheme

1. *The constant velocity rotating cup (RC) viscometer*

Because there is a lack of an explicit flow field solution (exact or numerical) of the OB configuration in the literature, we first use the exact solution of the RC viscometer [17] to benchmark our numerical model. By choosing appropriate boundary conditions it is straightforward to apply our scheme to the instrument design proposed and analyzed by Oh *et al.* [17]. In such a device, the cup containing the sample is forced to rotate at a constant angular velocity Ω, while the bicone is attached to a torsion wire. As a consequence of, both, the subphase and surface drags, the bicone will become stationary at a new equilibrium angular position, from which one can calculate the torque imposed by the flow field on the bicone. Oh *et al.* derived an exact solution of the Navier-Stokes equation for this configuration. Besides the approximations enumerated in the Section II C, Oh *et al.* considered Newtonian liquids and neglected inertial effects with respect to viscous effects. Under such conditions, the azimuthal velocity at the interface is given by [17]

$$\bar{v}_\theta = -\sum_{i=1}^{\infty} \frac{1}{\xi_i^2} \frac{A_i}{Bo} \left\{ J_1(\xi_i \bar{r}) - \frac{\bar{R}_1}{\bar{r}} \left(\frac{1-\bar{r}^2}{1-\bar{R}_1^2} \right) J_1(\xi_i \bar{R}_1) \right\} - \frac{\bar{R}_1^2}{\bar{r}} \left(\frac{1-\bar{r}^2}{1-\bar{R}_1^2} \right), \tag{22}$$

where the normalization of the azimuthal velocity in Ref. [17] is

$$\bar{v}_\theta = \frac{v_\theta}{R\Omega} - \bar{r}. \tag{23}$$

Moreover, J_1 is the first order Bessel Function of the first kind, ξ_i is the i-th zero of J_1, and A_i are coefficients given by

$$A_i = \frac{2\xi_i}{\tanh(\xi_i \bar{h}) J_0^2(\xi_i)} \left\{ \int_{\bar{R}_1}^{1} r' J_1(\xi_i r') \bar{v}_\theta(r')\, dr' - \frac{1}{\xi_i} \bar{R}_1^2 J_2(\xi_i \bar{R}_1) \right\}. \tag{24}$$

This elegant solution allows one to calculate the velocity profile at the interface and the total torque on the bicone with no need for solving the complete flow field. However, Eq. 22 is also an implicit equation and a numerical scheme is necessary to solve it. In that purpose, Oh *et al.* proposed an iterative procedure, using a mesh with 100 nodes at the interface. Starting from a first estimate for $\bar{v}_\theta$, the coefficients A_i are calculated from Eq. 24, and a corrected profile for $\bar{v}_\theta$ is then calculated from Eq. 22. This iteration is repeated until convergence is reached. Once $\bar{v}_\theta$ is known, the total torque on the bicone can be calculated

as [17]

$$\bar{T} = -\sum_{i=1}^{\infty} \left\{ \frac{A_i}{\xi_i^2} 2\bar{R}_1 \frac{J_1(\xi_i \bar{R}_1)}{1-\bar{R}_1^2} \right\} + \frac{2\bar{R}_1^2 Bo}{1-\bar{R}_1^2}, \tag{25}$$

where the torque is normalized as indicated in Eq. 17 recasting $\theta_0 e^{i\omega t}$ as Ω.

Eq. 22 can also be solved through a different numerical approach. Dividing the interface in a mesh with 100 nodes, we can substitute the integration in Eq. 24 by its numerical approximation (using, for instance, the trapezoidal rule). Then, the substitution of Eq. 24 into Eq. 22 yields a 100 by 100 system of linear equations. Finally, because the boundary conditions are known, the number of equations equals the number of unknowns and the linear system can be directly solved without the necessity of an iterative procedure. Hence we have two different ways to solve numerically the Oh *et al.* problem (Eqs. 22 and 24), and we want to compare their results with those obtained from the numerical solution of Eq. 4 with $\omega = 0$ and appropriate boundary conditions for the RC system. In this case, the azimuthal velocity is fixed at the cup rim, it has a linear radial profile at the cup bottom, and it is null at the conical bob surface and at the symmetry axis. In terms of the azimuthal velocity amplitude function these boundary conditions read

$$\begin{aligned} &g(1, \bar{z}) = 1, \\ &g(\bar{r}, 0) = \bar{r}, \\ &g(\bar{r} \leq \bar{R}_1, \bar{h}) = 0, \text{ and} \\ &g(0, \bar{z}) = 0. \end{aligned} \tag{26}$$

The boundary condition at the air-water interface is again defined by Eq. 8. Notice that, in this case (non oscillatory motion) $g(\bar{r}, \bar{z})$, Bo, and η must have only real parts. The corresponding torque balance expression has to be modified, so that, once $g(\bar{r}, \bar{z})$ is known, the non−dimensional total torque imposed by the subphase and the surface on the conical bob after all transients have decayed is

$$\bar{T} = \bar{T}_{\text{sub}} + \bar{T}_{\text{surf}} = -\int_0^{\bar{R}_1} \bar{r}^2 \left(\frac{\partial g}{\partial \bar{z}} \right)\Big|_{\bar{z}=\bar{h}} d\bar{r} + \bar{R}_1^2 Bo \left(\frac{\partial g}{\partial \bar{r}} \right)\Big|_{\bar{r}=\bar{R}_1, \bar{z}=\bar{h}}. \tag{27}$$

Incidentally, $\omega = 0$ means that ℓ_ω^s and ℓ_ω tend to infinity, which merely means that the relevant length scales for the linear momentum diffusion are the interface width and the subphase, respectively.

TABLE I: Values of the non−dimensional torque, $\bar{T}$, obtained, respectively, through the Oh *et al.* numerical scheme for solving Eq. 22 (Table I of [17]), our numerical approach to solve Eq. 22 through a system of linear equations (S.L.E.), and the procedure based on the full numerical solution of the flow field equation (Eqs. 4, 26, and 27) through a forward and backward second order finite differences method (F.B.F.D.). The geometrical parameters are $\bar{R}_1 = 0.8536$ and $\bar{h} = 0.2252$.

Bo	Ref. [17]	Eq. 25 (S.L.E.)	Eq. 27 (F.B.F.D.)
10	54.74	54.74	54.80
1	6.407	6.405	6.423
0.1	1.559	1.557	1.555

A quantitative comparison can be made through the comparison of the total torque on the bob. The results obtained through the three schemes for the values of the geometrical parameters given in [17] are summarized in the Table I. As can be seen, both numerical approaches based on the Oh *et al.* exact solution and our scheme based on the fully numerical solution of the flow field equations are in good agreement, with deviation of less than 1% in any case. The good agreement between the here proposed scheme based on the numerical solution of the flow field equations (Eq. 4) and the exact solution for the RC system [17] allows us to assume the accuracy of the numerical scheme to explore different configurations (as the RB, OC or OB systems) by just imposing the proper boundary conditions.

It is illustrative to analyze under which conditions the RC and the RB viscometers are equivalent. In other words, under which conditions Eqs. 22 and 25 proposed by Oh *et al.* for the RC system can be directly adapted to the RB system, as stated in Ref. [10]. We can, again, rewrite the boundary conditions and explicitly solve Eq. 4. Regarding the boundary conditions for the RB system, the velocity is null along the symmetry axis, and at the cup wall and bottom. Moreover, it increases linearly along the radial direction under the bob

surface. Hence, the boundary conditions for the RB configuration are

$$\begin{aligned} &g(1,\bar{z}) = 0, \\ &g(\bar{r},0) = 0, \\ &g(\bar{r} \leq \bar{R}_1, \bar{h}) = \bar{r}, \text{ and} \\ &g(0,\bar{z}) = 0. \end{aligned} \tag{28}$$

The velocity profiles at the interface for the boundary conditions given in Eqs. 28 and 26 are compared in Fig. 4 for $Bo = 0.02$. It can be seen that the velocity gradient is higher at the conical bob edge, regardless whether the rotating element is the cup or the bob. In addition, the solid curves in Fig. 4 represent the radial derivative of the interfacial velocity for the RB and RC systems, given by $(\partial g/\partial \bar{r} - g/\bar{r})\bar{R}_x$, where $\bar{R}_x = 1$ for the RC system, and $\bar{R}_x = \bar{R}_1$ for the RB system. These curves perfectly superimpose on top of each other, demonstrating that the RB and RC systems are equivalent in terms of the torque measured on the conical bob. Moreover, we have calculated the non−dimensional torque for the RB system as a function of Bo, and it exactly reproduces the values shown in the last column of Table I. Thus, the RB and RC systems (for which the azimuthal velocity is constant and, in consequence, there is no inertial contribution) are equivalent, and the torque measured on the conical bob does not depend on whether the rotating element is the cup or the bob.

2. The oscillating cup vs oscillating bob rheometers

Oscillatory shear experiments allow one to analyze the rheological response of the interface from a different perspective than the constant rotation viscometry experiments. Indeed, they yield a nice separation of the elastic and viscous components of the interface response. In consequence, several designs of interfacial rheometers based on bicone geometries with the capability of imposing an oscillatory shear stress on the interface have been reported. These devices may be classified into two main groups: i) Oscillating cup devices, in which the cup containing the sample is forced to perform an oscillatory motion while the effect of the total drag on the bicone is measured through its angular displacement (OB-OC systems) [18, 23], and ii) Oscillating bob devices, in which, both, imposing the external torque and measuring the angular displacement are performed on the biconical bob (OB systems) [10].

A general comment regarding the resolution of this type of instruments is in order here.

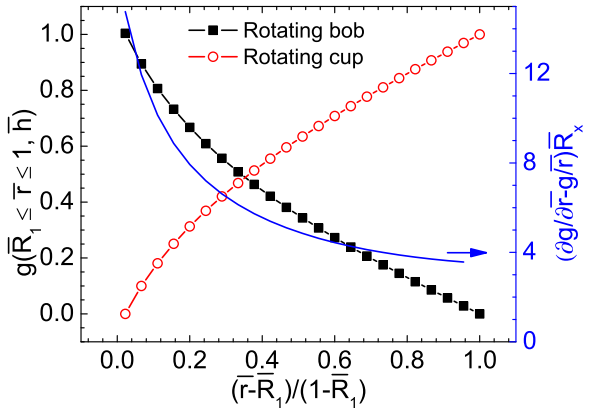

FIG. 4: Velocity profile at the interface calculated from the numerical solution of Eq. 4 for $\omega = 0$ and the boundary conditions given by Eqs. 26 (open circles) and 28 (filled squares). The Boussinesq number is $Bo = 0.02$ and the geometrical parameters are those described in the Section II A. The right vertical axis represents the radial derivative of the interfacial velocity, $(\partial g/\partial \bar{r} - g/\bar{r})\bar{R}_x$, where $\bar{R}_x = 1$ for the RC system, and $\bar{R}_x = \bar{R}_1$ for the RB system. These two curves superimpose on top of each other, yielding a single curve (blue solid line).

It has been shown [18] that, for those devices in which the external torque is imposed on the cup while the subsequent oscillatory displacement is measured on the bob, the ratio of the bob displacement amplitude to the cup displacement amplitude vanishes for low values of the complex viscosity or high frequencies. From Eq. 10 we know that the characteristic length at which the interfacial momentum is attenuated, $\bar{\ell}^s_\omega$, is proportional to $\left(|\eta^*_s|/\omega^{1/2}\right)^{1/2}$. The distance $\bar{\ell}^s_\omega$ satisfies $\bar{\ell}^s_\omega \ll 1 - \bar{R}_1$ in the regime of low values of $|\eta^*_s|$ and high values of ω. In the OB-OC configuration under these conditions, the cup momentum is attenuated in the vicinity of the cup wall, while the measurement of the angular displacement is conducted on the conical bob. Hence, the resolution in the angular position of the bob will be a strong limitation in the measurements, unless the interface is subjected to very high strains in the vicinity of the cup wall. In other words, one should expect the OB systems to be more precise than the OB-OC ones because both the forcing torque and the measurement of the angular displacement are conducted on the same element, the conical bob. This fact has made high precision rotational rheometers a preferred choice as base systems upon which to implement interfacial shear rheometers with conical bob fixtures.

A major contribution to the development of oscillating bob interfacial rheometers was made by Erni *et al.* [10]. Briefly, they adapted the model developed by Oh *et al.* [17] (Eqs. 22 and 24) to the OB system by imposing appropriate boundary conditions on Eq. 22, and recasting the constant angular velocity (Ω in the Oh *et al.* solution) as $\Omega(t) = \phi_0 e^{i\omega t}$. However, adapting the Oh *et al.* solution for the RC system to the case of the OB system is, in principle, not trivial. Indeed, the original Oh *et al.* solution corresponds to the boundary conditions of the RC system and they are implicitly included in the solution represented by Eq. 22.

Thus, two main concerns arise regarding the calculation of the OB system velocity profile from the adaptation of the RC system solution. First concern is related to fluid inertia. Observe that the fluid density, ρ, does not intervene in Eqs. 22, 24, and 25, so that fluid inertia is neglected in the Oh *et al.* solution. Because the oscillatory problem involves fluid accelerations and in most cases the subphase is made of low viscosity liquids, this approximation has to be taken with care. Second, using Eq. 22, which pertains to a moving cup problem, as a solution for the flow field of a moving bob problem is non trivial. Indeed, we have shown (see Fig. 4) that the flow fields for the moving cup and moving bob are equivalent for the constant angular velocity rotation problem, i.e., when all transients have decayed. However, we have shown also (see Fig. 2) that this is not the case for the oscillating cup and oscillating bob problems, particularly when low viscosities are involved. In other words, OB and OC systems should be equivalent only if the oscillation period is much longer than all of the characteristic times of the problem including those introduced by fluid inertia. Hence, the interplay of inertia and acceleration in the oscillatory problem deserves a careful analysis in order to clarify when OC and OB systems are equivalent.

To illustrate the differences between both, OB and OC systems, we have numerically solved the flow field equations for, on the one hand, the OB system, i.e., Eqs. 4, 7, and 18, and, on the other hand, the OC system, which are Eq. 4 with the following boundary conditions

$$\begin{aligned} &g^*(1, \bar{z}) = 1, \\ &g^*(\bar{r}, 0) = \bar{r}, \\ &g^*(0, \bar{z}) = 0, \text{ and} \\ &g^*(\bar{r} \leq \bar{R}_1, \bar{h}) = 0. \end{aligned} \tag{29}$$

The velocity profile at the interface for the OB and the OC systems are shown in Figs. 2a-2b and 2c-2d, respectively. As it was mentioned in the Section II C, the shape of the curves corresponding to the OB and OC configurations differ when $\bar{\ell}_\omega^s \ll 1-\bar{R}_1$, allowing one to expect that, when the characteristic length of the system is $\bar{\ell}_\omega^s$ instead of $1-\bar{R}_1$, the torque on the conical bob depends on whether the oscillating part is the cup or the bob. We have quantitatively compared the torques for both systems, where the torque corresponding to the OB system is given by Eqs. 15, while the torque corresponding to the OC system can be calculated from the summation of the torques due to the subphase and the surface drags, which are given, respectively, by the following expressions

$$\begin{aligned} T^*_{\text{sub}} &= -\int_0^{\bar{R}_1} \bar{r}^2 \left(\frac{\partial g^*}{\partial z}\right)\Big|_{\bar{z}=\bar{h}} d\bar{r}, \\ T^*_{\text{surf}} &= \bar{R}_1^2 Bo^* \left(\frac{\partial g^*}{\partial \bar{r}}\right)\Big|_{\bar{r}=\bar{R}_1,\bar{z}=\bar{h}}. \end{aligned} \tag{30}$$

The comparison of the total torque for both systems is shown in Fig. 5, where the solid curves correspond to the OB system and the dashed curves correspond to the OC system. More precisely, in Fig. 5 we represent the modulus and the argument of the total non−dimensional torque on the bob versus $|Bo^*|$ for three different ω and $\arg(Bo^*)$ combinations that represent three different characteristic cases: (a) $f = 0.05\,\text{Hz}$ and a purely elastic surface, (b) $f = 0.5\,\text{Hz}$ and a viscoelastic surface, $\eta_s' = \eta_s''$, and (c) $f = 5\,\text{Hz}$ and a purely viscous surface. All of the curves correspond to the same set of geometrical parameters described in the Section II A (see supplementary material for results on other combinations of ω and $\arg(Bo^*)$).

As expected, the total torque on the bob for both systems coincides at high values of $|Bo^*|$, at which $\bar{\ell}_\omega^s \gg 1-\bar{R}_1$ and the interface velocity is linear in $\bar{r}$, while they clearly separate for lower values of the complex Boussinesq number, for which $\bar{\ell}_\omega^s \ll 1-\bar{R}_1$ and $\bar{\ell}_\omega^s$ is the characteristic length scale. Moreover, in the OC configuration, $\left|\bar{T}^*\right|$ remarkably decreases upon decreasing $|Bo^*|$, which is in agreement with the behavior mentioned in [18]. Thus, these results reinforce the arguments above explained: i) Systems based on a OB configuration are expected to be more sensitive, and ii) the two different systems are not, in general, equivalent, so that interpreting the OB results by recasting of the Oh *et al.* solution for the OC system will definitely fail when the distance at which the interface momentum is attenuated, $\bar{\ell}_\omega^s$, is comparable or smaller than $1-\bar{R}_1$. If this is the case, the interface velocity decays in the vicinity of the mobile element, and the OC and OB systems are necessarily

non-equivalent.

For purposes that will be apparent later, we will label as $|Bo^*|^{\text{th}}_{\text{OC}-\text{OB}}$ the threshold value at which $\arg(\bar{T}^*)$ bifurcates in different curves for the OC and the OB configurations in Fig. 5.

B. Implementation of an oscillating conical bob interfacial rheometer on a Bohlin C-VOR torsional rheometer

1. Estimating the ultimate resolution of an oscillating conical bob rheometer

Once we have discussed the performance of our numerical approach at some benchmark cases, we will now turn to the application of this approach onto the oscillating conical bob rheometer. Actually, we are now in position to estimate the ultimate resolution of such devices taking into account the resolution in the measurements of torque, ΔT, and angular position, $\Delta\theta$, of the rotational rheometer in which the conical bob is installed.

It is important to notice, however, that a detailed error analysis, such as the one performed in [12] for the magnetic tweezers ISR, is not possible in the case of a home made conical bob system mounted on a standard rotational rheometer because of incomplete information about technical details of the rheometer such as the discrete Fourier transform algorithm used in the rotational rheometer control software to calculate, both, the amplitude ratio and the phase lag.

An alternative approach can be setup by realizing that, in order to be able to measure the dynamic surface moduli of an interface, we need the corresponding experimental amplitude ratio, AR^*_{exp}, to be distinguishable from the amplitude ratio corresponding to a clean air-water interface, AR^*_{clean}. In other words, only those dynamic surface moduli for which the difference $AR^*_{\text{exp}} - AR^*_{\text{clean}}$ is higher than the resolution of the device can be measured. Hence, making a statistical analysis of the dispersion of the experimental values of the amplitude ratio and the phase lag obtained for a clean air-water interface we can setup a criterion that will tell us when the values obtained for the interface under study can be distinguished from those corresponding to a clean air-water interface.

Consequently, we have performed a statistical analysis of the experimental values of the amplitude ratio modulus, $|AR^*_{\text{clean}}(f)|$, and phase angle, $\delta_{\text{clean}}(f)$, at three different frequen-

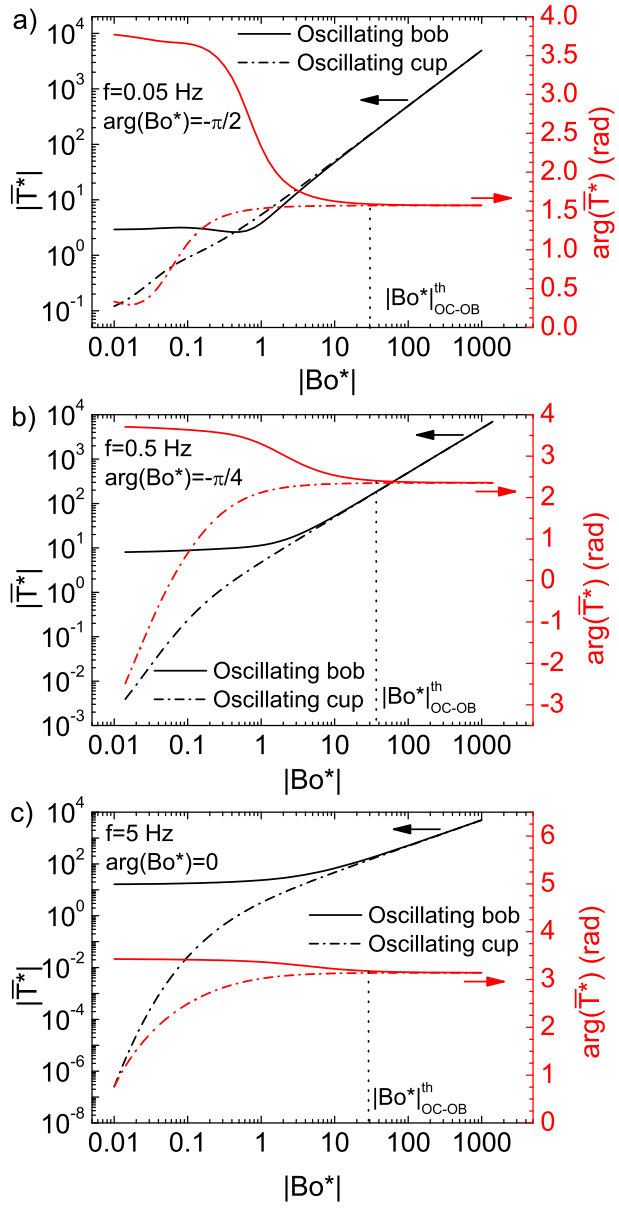

FIG. 5: Comparison of the non−dimensional torque modulus, $|\bar{T}^*|$ (left vertical axis), and $\arg(\bar{T}^*)$ (right vertical axis) versus $|Bo^*|$, for two systems: stationary cup-oscillating bob (solid curves), and oscillating cup-stationary bob (dashed curves). Three representative cases are shown: a) $f = 0.05\,\mathrm{Hz}$ and purely elastic interface, $\arg(Bo^*) = -\pi/2\,\mathrm{rad}$, b) $f = 0.5\,\mathrm{Hz}$ and viscoelastic interface, $\arg(Bo^*) = -\pi/4\,\mathrm{rad}$, c) $f = 5\,\mathrm{Hz}$ and purely viscous interface, $\arg(Bo^*) = 0$. See supplementary material for results on other combinations of f and $\arg(Bo^*)$.

cies, f, in the range $0.05 \leq f \leq 5$ Hz. At each oscillation frequency, the rheometer was set to make 360 consecutive measurements, each of them for a time lapse of one oscillation period. In all cases the probability densities were well represented by Gaussian functions (see Figs. 6a and 6b for $f = 0.5\,\mathrm{Hz}$), and the corresponding standard deviations, $\sigma(|AR^*_{\mathrm{clean}}|)$, and $\sigma(\delta_{\mathrm{clean}})$, are represented in Fig. 6c versus frequency. The criterion that we used in our experiments to accept and compute an experimentally measured amplitude ratio is that it must satisfy

$$\begin{aligned} \left| \left| AR^*_{\mathrm{exp}} \right| - |AR^*_{\mathrm{clean}}| \right| &\geq \sigma\left(|AR^*_{\mathrm{clean}}|\right), \\ |\delta_{\mathrm{exp}} - \delta_{\mathrm{clean}}| &\geq \sigma\left(\delta_{\mathrm{clean}}\right). \end{aligned} \tag{31}$$

In Fig. 7 we represent the differences between the modulus (solid curves, left vertical axes) and arguments (dashed curves, right vertical axes) of the amplitude ratios corresponding to interfaces with dynamic moduli given by $|Bo^*|$ and a clean air-water interface. The geometrical parameters used in this calculation are those given in Section II A and the values of the frequency and $\arg(Bo^*)$ are the same as in the three cases studied in Fig. 5 (more frequency and $\arg(Bo^*)$ combinations are shown in the supplementary material).

The scales of the vertical axes have been chosen in such a way that the standard deviations, $\sigma(|AR^*_{\mathrm{clean}}|)$ and $\sigma(\delta_{\mathrm{clean}})$ are represented by the same horizontal dotted curve. Thus, the range of measurable dynamic surface moduli is the region in which the curves representing $\left| \left| AR^*_{\mathrm{exp}} \right| - |AR^*_{\mathrm{clean}}| \right|$ and $|\delta_{\mathrm{exp}} - \delta_{\mathrm{clean}}|$ are above the dotted lines.

Several facts can be observed in Fig. 7. First, for the vertical scales chosen in Fig. 7, the modulus difference lays below the phase lag difference for all the explored $f - \arg(Bo^*)$ combinations. Hence, for the device used in these experiments, the resolution in the modulus of the amplitude ratio appears to be the limiting factor in all cases. Second, resonant like phenomena related to the elastic modulus of the interfaces are seen as regions in which $\left| AR^*_{\mathrm{exp}} \right| - |AR^*_{\mathrm{clean}}| < 0$. Unless the elastic modulus is negligible with respect to the loss modulus, there is a value of $|Bo^*|$ for which $\left| AR^*_{\mathrm{exp}} \right| = |AR^*_{\mathrm{clean}}|$, that appears as a *blind* region (see the inverted peaks in Fig. 7a around $|Bo^*| = 10$, and Fig. 7b around $|Bo^*| = 50$). For values of $|Bo^*|$ on the left of these inverted peaks, the difference of amplitude ratios verifies $\left| AR^*_{\mathrm{exp}} \right| - |AR^*_{\mathrm{clean}}| < 0$. In other words, for these values of $|Bo^*|$ the torque needed to shear the monolayer is lower than that corresponding to a clean interface. This behavior

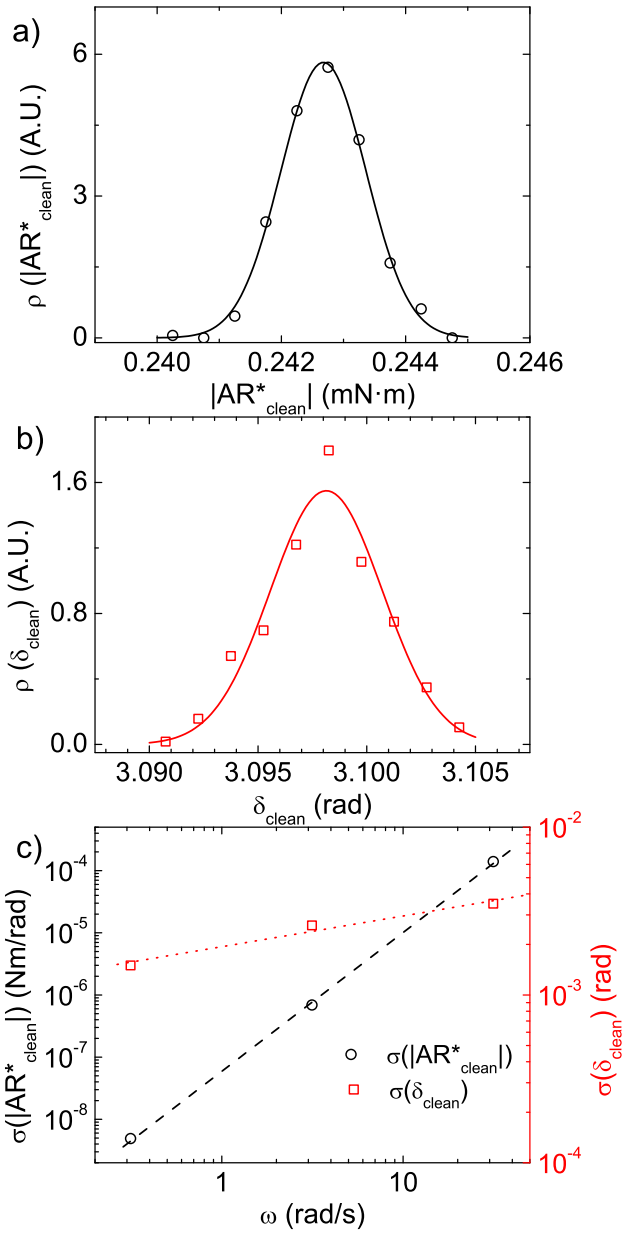

FIG. 6: Probability density measured on a clean air-water interface for $|AR^*_{\rm clean}|$ (a), and $\delta_{\rm clean}$ (b) corresponding to a frequency $f = 0.5\,$Hz. The solid curves represent the fit of the experimental data to a Gaussian function. c) Value of the standard deviations, $\sigma(|AR^*_{\rm clean}|)$, and $\sigma(\delta_{\rm clean})$, versus frequency.

can be explained as a resonance effect due to the elastic modulus of the interface.

These resonance phenomena are well known to appear in controlled stress rotational rheometers when working with weak samples. Then rotor inertia couples with the sample's viscoelastic properties to induce such resonances. For instance Baravian *et al.* [24]

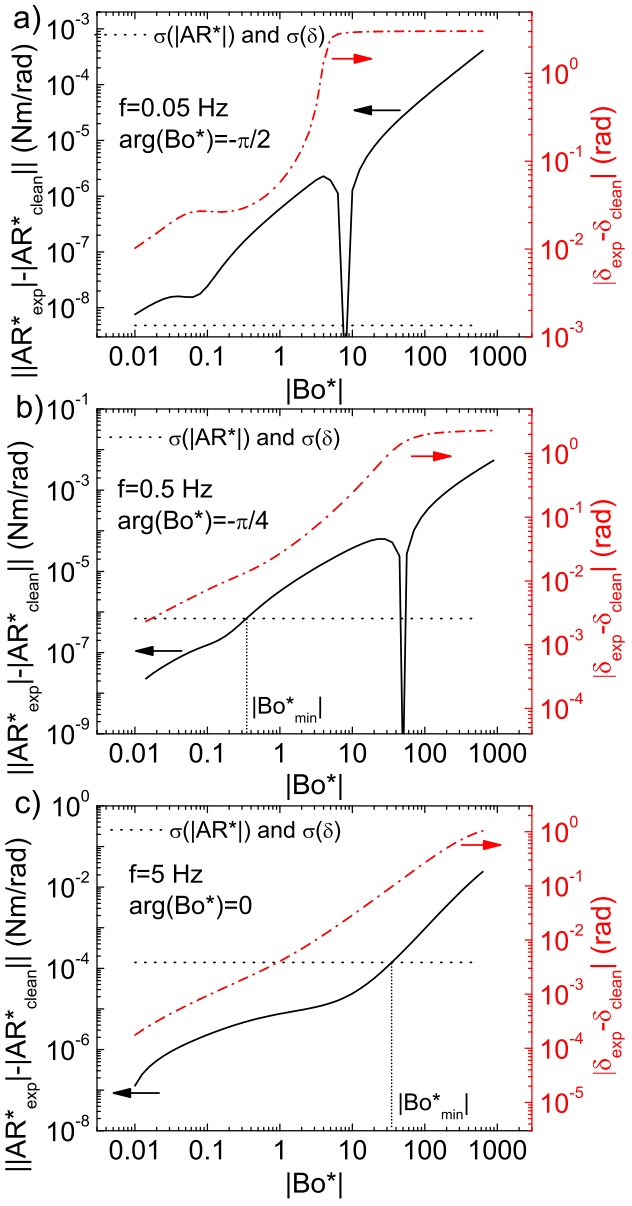

FIG. 7: Differences between the modulus (solid curves, left vertical axis) and the phase lag (dashed curves, right vertical axis) of the amplitude ratios corresponding to an interface with dynamic surface moduli given by $|Bo^*|$ and a clean air-water interface (geometrical parameter values given in Section II A). The scale of the vertical axes has been tuned so that the resolution in amplitude ratio, $\sigma(|AR^*_{\rm clean}|)$, and phase lag, $\sigma(\delta_{\rm clean})$, is represented by the same dotted curve. Cases (a), (b), and (c) correspond to the same values of frequency and $\arg(Bo^*)$ as in Fig. 5. See supplementary material for results on other combinations of f and $\arg(Bo^*)$.

thoroughly studied the case of a Maxwell-Jeffreys fluid in a rotational rheometer both in creep and oscillatory measurements. They showed that resonance occurs when the effective shear stress exerted on the sample significantly differs from the shear stress corresponding to the torque applied to the rotor because of rotor inertia effects. Moreover, in Ref. [24] a non-vanishing sample elasticity was needed for the resonance to appear. This characteristic is observed too in Fig. 7, where no resonance appears for the c) case, namely a purely viscous interface. Deriving a criterion for the resonance occurrence is challenging because, for instance, in bulk rotational rheometry one would need to know the sample's constitutive equation. In the case of the interfacial rotational shear rheometers (either with bicone, du Noüy ring, or double wall ring fixtures) the difficulty increases because one would need to know the subphase and interface constitutive equations, and the flow field solution because of the coupling at the interface through the Boussinesq-Scriven boundary condition.

Notice that, even when this resonance takes place, it is possible to measure the dynamic surface moduli as long as $\left||AR^*_{\rm exp}| - |AR^*_{\rm clean}|\right| > \sigma(|AR^*_{\rm clean}|)$. Third, let us label as $|Bo^*|_{\rm min}$ the minimum measurable value of $|Bo^*|$, i. e., the value at which the dotted and solid curves cross each other in Fig. 7. While $|Bo^*_{\rm min}| \simeq |Bo^*|^{\rm th}_{\rm OC-OB}$ for the case (c) in Figs. 5 and 7, it is clear that $|Bo^*_{\rm min}| \ll |Bo^*|^{\rm th}_{\rm OC-OB}$ for the cases (a) and (b). Hence, the resolution of the rotational rheometer allows one to distinguish interfaces with dynamic surface moduli so low that the explicit resolution of the velocity profile of the OB system is required if one wants to exploit the full resolution of the rotational rheometer.

2. When is the explicit calculation of the velocity profile mandatory?

Because the complexity of the procedure and the computational cost for analyzing the experimental data through the solution of the flow field is significantly higher than any calculation of the dynamic surface moduli using an analytic expression, one may wonder under which conditions the explicit calculation of the velocity profile is mandatory and the simplest approximations must be avoided. In that purpose we have compared the data processing here proposed with a simpler (and more efficient in terms of computational cost) method derived following Ref. [25]. Let us assume that the velocity profile at the interface is linear. Then, from the strain tensor in cylindrical coordinates, the amplitude of the shear

strain at the conical bob edge is

$$\gamma_0 = \left| \left(\frac{\partial u_\theta}{\partial r} - \frac{u_\theta}{r} \right) \Big|_{r=R_1} \right| = \theta_0 \frac{R}{R - R_1}, \tag{32}$$

where u_θ is the azimuthal displacement. The amplitude of the shear stress, calculated as the force applied along the conical bob edge, is given by

$$\sigma_0 = \frac{T_0}{R_1} \frac{1}{2\pi R_1}. \tag{33}$$

Then, the dynamic surface moduli can be calculated as

$$G_s^* = G_s' + iG_s'' = \frac{\sigma_0}{\gamma_0} e^{i\delta} = \frac{R - R_1}{2\pi R_1^2 R} AR_s^*, \tag{34}$$

where AR_s^* is the amplitude ratio due to the surface drag (that amplitude ratio that we would measure in the absence of any other contribution). If we assume that the surface drag and the rest of contributions to the conical bob dynamics are simply additive, we can calculate the dynamic surface moduli as

$$G_s^* = \frac{R - R_1}{2\pi R_1^2 R} \left(AR_{\text{exp}}^* - AR_{\text{clean}}^* \right). \tag{35}$$

The calculation of G_s^* from the raw data using Eq. 35 is immediate. Thus, it is convenient to determine under which conditions the linear approximation represented by Eq. 35 is a good enough approximation. In that purpose, consider a surface with a given complex Boussinesq number, Bo^*, yielding a complex amplitude ratio, AR_{theo}^*, given by Eq. 18. If the approximation above mentioned is good enough, the substitution of AR_{theo}^* on Eq. 35 as AR_{exp}^* would give a value for G_s^* yielding an apparent complex Boussinesq number, Bo_{app}^*, which should be in good agreement with the initial one. On the contrary, if the actual flow field is not well represented by the linear approximation or the simple addition of the surface drag and the rest of contributions fails, the initial Bo^* and the apparent Bo_{app}^* would be different.

In Fig. 8 we compare the value of $\left|Bo_{\text{app}}^*\right|$ with the initial $|Bo^*|$ for the same three frequencies and $\arg(Bo^*)$ as in Figs. 5 and 7 (see supplementary material for more frequency and $\arg(Bo^*)$ combinations). The solid curves represent the ratio $\left|Bo_{\text{app}}^*\right| / |Bo^*|$, and the dashed curves the difference $\arg(Bo_{\text{app}}^*) - \arg(Bo^*)$. The vertical dotted lines represent the value of $|Bo_{\text{min}}^*|$. As the value of the complex Boussinesq number of the surface decreases, the apparent value obtained through the linear approximation separates from the actual value.

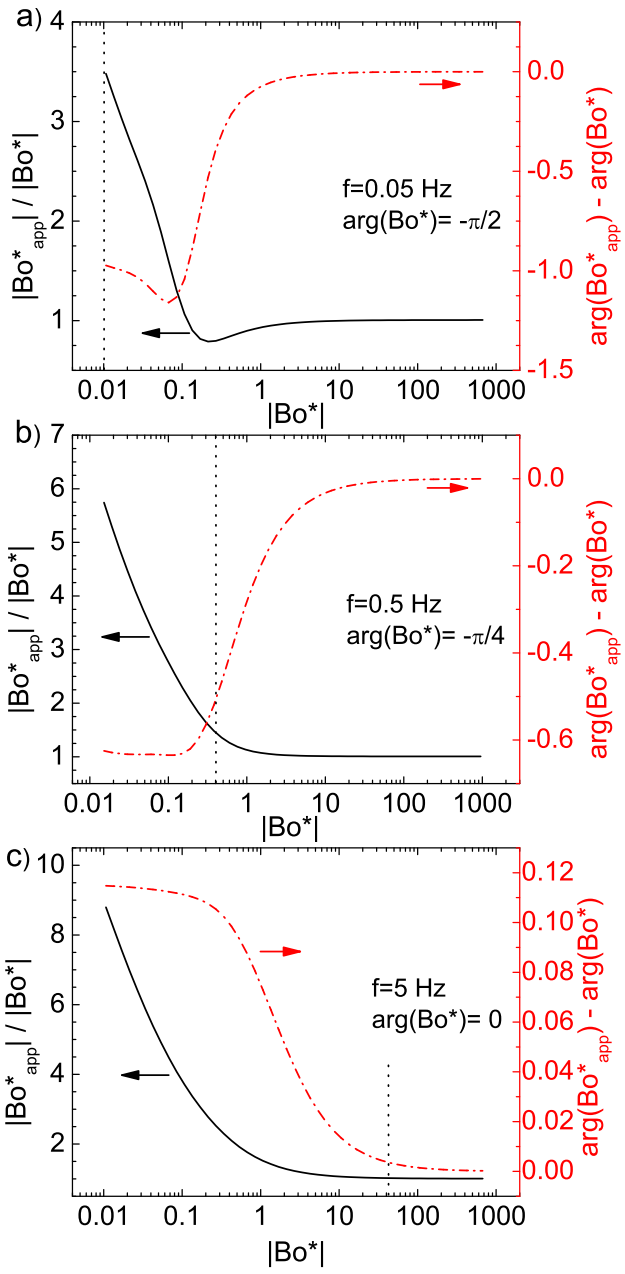

FIG. 8: Comparison of the performance of two data processing schemes: one based on the assumption of a linear velocity profile (Eq. 35), and the other one based on the numerical resolution of the Navier-Stokes equation (Eq. 18). From the same torque and phase lag initial data, we calculate $Bo^*_{\rm app}$ through Eq. 35 and Bo^* through Eq. 18. The solid and dashed curves represent the ratio $\left|Bo^*_{\rm app}\right| / \left|Bo^*\right|$ and the difference $\arg(Bo^*_{\rm app}) - \arg(Bo^*)$ versus $|Bo^*|$, respectively. The vertical dotted curves represent $|Bo^*_{\rm min}|$, extracted from Fig. 7. Cases (a), (b), and (c) correspond to the same values of frequency and $\arg(Bo^*)$ as in Figs. 5 and 7. See supplementary material for more frequency and $\arg(Bo^*)$ combinations.

Indeed, in the cases of Figs. 8a and 8b, there is a wide region of Boussinesq number values satisfying $|Bo^*| > |Bo^*_{\min}|$, i.e., that are, in principle, measurable, for which the assumption of the linear approximation would yield a remarkable error in the analysis of the raw data. In the case of Fig. 8a, $\left|Bo^*_{\rm app}\right|$ can be overestimated in more than three times, while $\arg(Bo^*_{\rm app})$ can separate in more than 1 rad from the actual one. In the case of Fig. 8b, while $\left|Bo^*_{\rm app}\right|$ can be only slightly overestimated in the measurable region, a remarkable difference can occur in $\arg(Bo^*_{\rm app})$, so that, while the value of $|G^*_s|$ can be acceptably recovered by the linear approximation, it will fail in the calculation of the ratio G'_s/G''_s. On the contrary, for higher frequencies (see Fig. 8c), $|Bo^*_{\min}|$ is right-shifted up to $|Bo^*| \simeq 40$, so that the linear approximation can be safely used provided that $|Bo^*_{\rm app}|$ and $|Bo^*|$ do not separate in the measurable region.

In consequence, from the curves in Fig. 8 (and Fig. 5 in the Supplementary Material) we can conclude that, for the low frequency regime, $\omega \simeq 0.05\,\text{Hz}$, the explicit calculation of the velocity profile is mandatory for $|Bo^*| \lesssim 1$ and the resolution of the device allows one to measure $|Bo^*|$ values as low as 0.01. In the case of the intermediate frequency range, $\omega \simeq 0.5\,\text{Hz}$, $|Bo^*|$ values down to 0.4 are measurable, and the linear approximation is good enough for $|Bo^*| \gtrsim 3$. Finally, for high frequencies, $\omega \simeq 5\,\text{Hz}$, the inertial term rules the dynamics of the system and the measurable region is right-shifted up to $|Bo^*| \gtrsim 40$. In other words, for high frequencies, only interfaces with high dynamic moduli show a contribution distinguishable from the inertial term, and the linear approximation is valid for the hydrodynamical description of the system.

Two final comments are in order here: First the inertia term in Eq. 18 is proportional to ω^2, so it inevitably dominates at high frequencies and the interface and the subphase contributions become irrelevant. Hence, the amplitude ratio will grow proportionally to ω^2 and the relative phase will tend to π. This can be used in experiments as a signature to easily recognize the rotor inertia dominated regime. Second, the possible occurrence of instabilities due to subphase motion can be discussed in terms of the Reynolds number. However, the above mentioned definition of the Reynolds number for rotational motion, $Re = (\rho\omega R^2)/\eta$, is not appropriate here because it amounts to consider ωR as the relevant velocity scale, which is not the case because, for the small amplitude oscillatory motion of the bicone, ω is the oscillation frequency, not the typical angular velocity. Actually, for the small amplitude oscillatory motion here considered, given an angular displacement of

amplitude θ_0, the corresponding arc length amplitude would be $\theta_0 R_1$, and the azimuthal velocity amplitude at the bicone edge is $\theta_0 R_1 \omega$, which is the appropriate velocity scale for a small amplitude oscillatory motion. Then, using Eq. 32, $Re = [\rho(R - R_1)R_1\gamma_0\omega]/\eta \simeq 200\,\gamma_0\,\omega$, approximately, for the configuration used here. Hence, in all of the frequency sweep experiments reported in the next section ($\gamma_0 \leq 0.01$), the Reynolds number values are in the range $1 \leq Re \leq 100$, while in the strain sweep experiments ($\omega = 0.5\,\mathrm{Hz}$) the Reynolds number values are in the range $0.5 \leq Re \leq 20$.

C. Experimental results

1. Purely viscous interfaces

We have first tested the performance of the device and the data processing scheme on purely viscous interfaces by measurements on thin films made of silicone oil. A controlled volume of silicone oil was spread on the air-water interface, and the rheological experiments were performed after waiting for 2 hours, in order to ensure a homogeneous film depth.

In Fig. 9 we show the results obtained for two different silicone oil films. Film 1 is a $150\,\mu$m depth layer of Fluka 85424 silicone oil having bulk viscosity $\eta_1 = 33\,\mathrm{Pa}\cdot\mathrm{s}$, which yields an expected interfacial viscosity of $\eta_{s,1} = 4.95 \times 10^{-3}\,\mathrm{N}\cdot\mathrm{s/m}$. Film 2 is a $100\,\mu$m deep layer of Fluka 85422 silicone oil having bulk viscosity $\eta_2 = 1\,\mathrm{Pa}\cdot\mathrm{s}$, which yields an expected interfacial viscosity of $\eta_{s,2} = 1 \times 10^{-4}\,\mathrm{N}\cdot\mathrm{s/m}$.

In Fig. 9a symbols represent the interfacial loss modulus, G_s'', as a function of the oscillation frequency for both silicone oil films, while the dotted lines represent their expected values. The storage modulus, G_s', is in all cases negligible with respect to G_s'' and lays out of the graph. The measurements have been made at a constant strain of 5 %, and the raw data corresponding to the thin film 2 at frequencies above 10 rad/s were discarded because the condition $\left|\left|AR^*_{\mathrm{exp}}\right| - \left|AR^*_{\mathrm{clean}}\right|\right| \geq \sigma\left(\left|AR^*_{\mathrm{clean}}\right|\right)$ was not satisfied (because the inertial term is proportional to ω^2, it can become the governing term for high frequencies and relatively low dynamic surface moduli). The agreement with the expected values is remarkable in the rest of the experimental results.

Conversely, in Fig. 9(b) the symbols represent the interfacial loss modulus, G_s'', as a function of the strain amplitude for both silicone oil films, while the dotted lines are their

expected values. The measurements have been made at a constant frequency $f = 0.5\,\mathrm{Hz}$. Again, the results of G_s' are much smaller, laying out of the graph. In addition, the experiments recover the expected results with good approximation though a higher measurement noise is apparent for the lower viscosity film.

As a comparison with the linear approximation discussed in the previous Section, we have processed the same experimental raw data using Eq. 35. The results are shown in Figs. 9c and 9d. As can be seen, the expected result for the higher viscosity film is nicely recovered, but, for the lower viscosity film, this method introduces a spurious G_s' of the same order of G_s''. The expected Boussinesq number for this thin film is $Bo^* = 2.5$. For a purely viscous interface with such a value of Bo^*, the apparent Boussinesq number obtained from the linear approximation is very similar to the actual Boussinesq number in modulus, but they separate in argument (see Fig. 5d in supplementary material). In other words, from the calculation of $\left|Bo^*_{\mathrm{app}}\right|$, one can expect that the linear approximation given by Eq. 35 recovers the actual value of G_s^* while it introduces spurious effects in G_s' and G_s''. This is exactly what is observed in Figs. 9c and 9d.

2. Fatty acid Langmuir monolayers

The performance of the conical bob rheometer was also tested through measurements on fatty acid Langmuir monolayers that allow for a comparison with results on similar systems obtained by means of a magnetic tweezers driven interfacial shear rheometer (ISR) [12]. It is known that fatty acid monolayers show a very rich behavior in terms of their temperature - surface pressure (Π) phase diagram [20] and their rheological response [26]. Several phases have been found, corresponding to different microscopic structures and showing clearly differentiated dynamic surface moduli. It is also known that phase diagrams for monolayers of fatty acids having different chain lengths can be superposed upon shifting the temperature by approximately 5°C for each extra carbon atom in the chain backbone [27]. Thus, this kind of one-molecule depth monolayers are an excellent benchmark of interfacial shear rheometers because a proper selection of temperature, chain length, and surface pressure allows one to have surfaces with the convenient rheological response. In the present study, we would like the monolayer to satisfy the following constraints: i) The surface viscosity must be in the range in which both, the conical bob rheometer and the ISR, can make precise me-

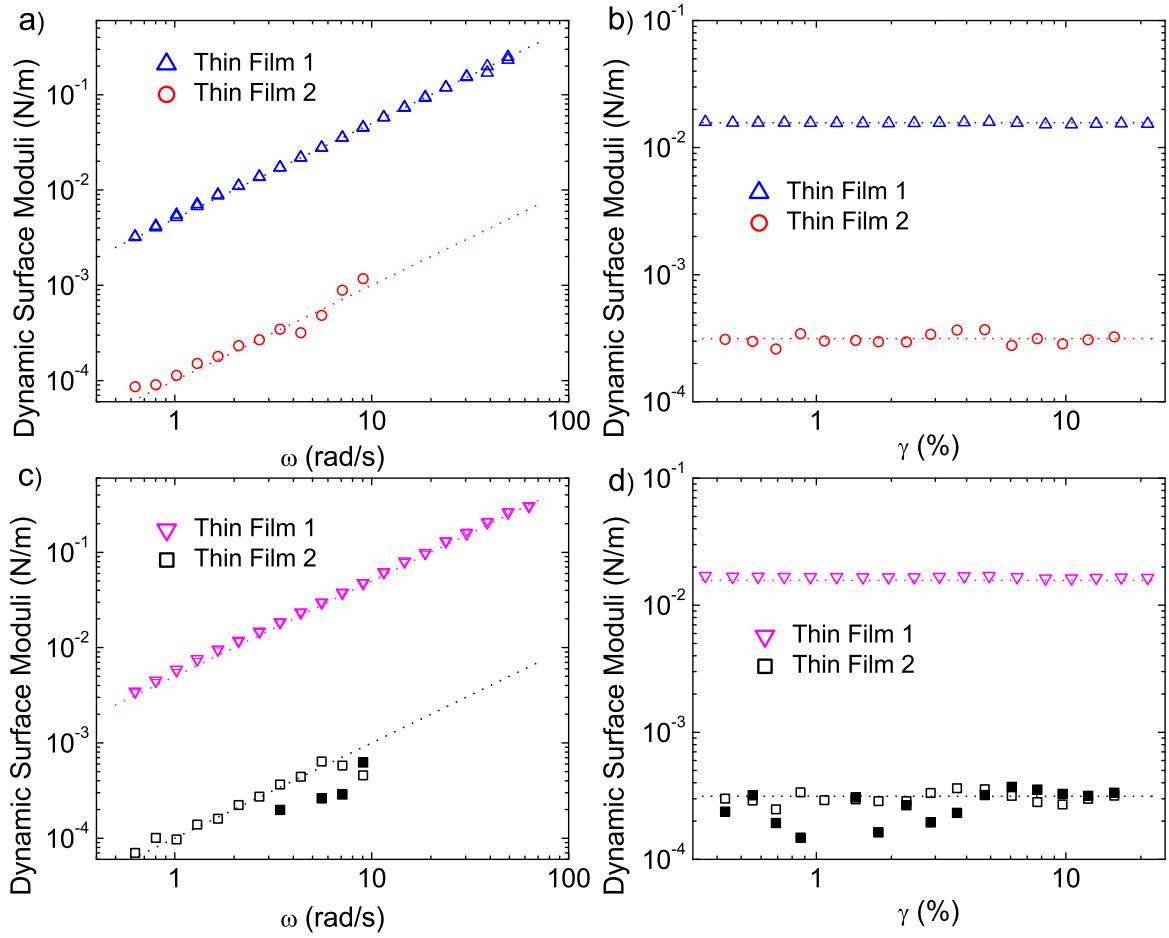

FIG. 9: Dynamic surface moduli versus frequency (a and c) and versus strain amplitude (b and d) obtained from measurements on two different silicone oil films with expected interfacial viscosities $\eta_{s,1} = 4.95 \times 10^{-3}\,\mathrm{N \cdot s/m}$, and $\eta_{s,2} = 1 \times 10^{-4}\,\mathrm{N \cdot s/m}$. Plots (a) and (b) represent the result of the data processing method described in the Section II D. Plots (c) and (d) represent the results of processing the same raw data using the linear approximation given by Eq. 35. The open symbols correspond to G_s'', and the filled symbols correspond to G_s' (G_s' is not represented in those cases in which G_s' is much lower than G_s'' and falls outside the plot).

asurements ($10^{-5}\,\mathrm{N\,s/m} \leq |\eta_s^*| \leq 10^{-2}\,\mathrm{N\,s/m}$), and ii) highly elastic surfaces are not useful because of the asymmetry of the measurement cell and the consequent possible appearance of heterogeneity in the surface pressure over the air-water interface [28]. Hence we have chosen to measure two different monolayers at room temperature: lignoceric acid (C24) at the L2 phase ($\Pi \lesssim 20\,\mathrm{mN/m}$), and pentadecanoic acid (C15) at the L2 ($\Pi \lesssim 20\,\mathrm{mN/m}$) and

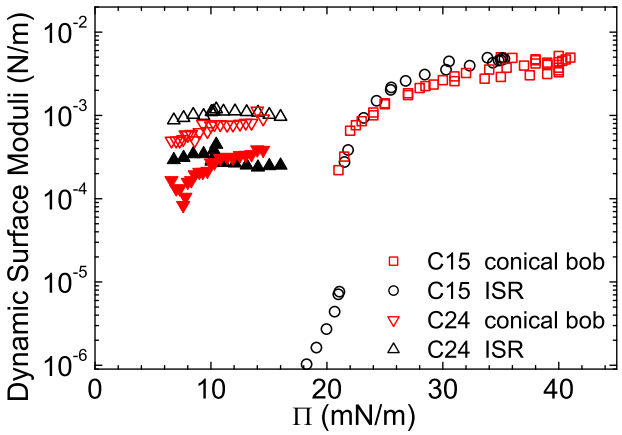

FIG. 10: Comparison of the conical bob and the ISR performance. Dynamic surface moduli versus surface pressure for two different fatty acids, pentadecanoic acid (C15) and lignoceric acid (C24), at room temperature. Filled symbols represent G_s', and open symbols represent G_s''. In the case of the C15 fatty acid, G_s' was negligible compared to G_s''.

LS ($\Pi \gtrsim 20\,\mathrm{mN/m}$) phases.

The result of the comparison of the ISR and the conical bob performance for both systems is shown in Fig. 10. In the case of the C24 fatty acid the results on G_s' and G_s'' from the ISR and the conical bob are in fair agreement over the whole L2 phase. The results for higher surface pressure values are not considered in this paper because the monolayer enters the CS phase (close packed solid), which is mainly elastic having a storage modulus higher than the upper limit of the ISR.

In the case of the C15 fatty acid, the storage modulus is not represented because it is negligible with respect to the loss mudulus and cannot be distinguished from the experimental data, regardless of the device used. As can be seen in Fig. 10, the results from the ISR and the conical bob nicely coincide at the LS phase, for $\Pi \gtrsim 20\,\mathrm{mN/m}$. However, the conical bob cannot reproduce the results from the ISR for lower surface pressure values (L2 phase), because for $\Pi \lesssim 20\,\mathrm{mN/m}$, we found that $\left|\left|AR^*_{\mathrm{exp}}\right| - \left|AR^*_{\mathrm{clean}}\right|\right| < \sigma(|AR^*|)$, so that the interface cannot be distinguished from a clean air-water interface.

The lower limit that we experimentally found in the measurements on the C15 fatty acid is in good agreement with the minimum measurable interfacial viscosity that can be estimated from the device resolution. Indeed, from Fig. 7b, one can conclude that the minimum $|Bo^*|$ measurable for $f = 0.5\,\mathrm{Hz}$ is around 0.4, which yields a minimum measurable complex

viscosity $|\eta_s^*| \simeq 1.6 \times 10^{-5}\,\mathrm{N \cdot s/m}$. The experimental results from the conical bob are in good agreement with those from the ISR as long as the surface viscosity is above this limit and the calculation of the velocity profile is used for the data processing. Interfaces with surface viscosity values below this limit can be precisely measured by other techniques such that microrheology [29] or magnetic tweezers ISR [12], but they are not measurable by the conical bob not because of the theoretical model used for the data processing, but because of the ultimate resolution of the rotational rheometer.

IV. CONCLUSIONS

We have studied, both theoretically and experimentally, the problem of setting up an interfacial rheometer by using a conical bob fixture in a conventional rotational rheometer, with particular emphasis on the data processing scheme. Other geometries such as double wall ring [8] or magnetic needles [25] are more sensitive due to their lower tool inertia, but the bicone geometry attached to a torsion rheometer is extensively used among the rheology researchers; the ease of fabrication of the accessories needed and the availability from several manufactures make the bicone geometry the chosen option in many laboratories.

We have devised a procedure based on numerically solving the fluid flow equations under suitable approximations and with proper boundary conditions, and using the flow profile to iteratively find a correction to the complex Boussinesq number in the same spirit of Refs. [6, 8, 9]. We calculate the flow profiles, both at the subphase and the interface, by numerically integrating the Navier-Stokes equation with a Boussineq-Scriven boundary condition at the interface by means of a second order forward and backward finite differences method in four different configurations: i) stationary conical bob - rotating cup at constant velocity (RC), ii) rotating conical bob at constant velocity - stationary cup (RB), iii) stationary conical bob - oscillating cup (OC), and iv) oscillating conical bob - stationary cup (OB).

For the RC configuration, the results on the total torque on the bob are in very good agreement with the exact solution proposed by Oh *et al.* [17]. Moreover, we have shown that, provided that the assumptions of the hydrodynamical model described in the Section II C are fulfilled and there are no instabilities, the RC and RB configurations are equivalent and the torque exerted on the conical bob does not depend on which the moving element is, provided all transients have decayed.

On the contrary, the OC and the OB configurations are not, in general, equivalent. Thus, a direct adaptation of the OC system solution to the OB problem is not recommended unless Bo^* is high.

We have used the here proposed numerical approach to build up a data processing method to be used in an interfacial shear rheometer made by supplying a conventional rotational rheometer with a conical bob fixture. We have shown that this data processing method allows for the calculation of the dynamic surface moduli from the torque and displacement raw data with a precision limited just by the instrument resolution.

The performance of this rheometer and data processing ensemble has been tested by experiments on silicone oil films and comparing the results with a simpler linear approximation for the data processing. The expected surface viscosity of the thin films is nicely recovered. Moreover, we have shown that, for the bicone interfacial rheometer, the linear approximation data processing, while yielding a correct value for the modulus of the complex dynamic modulus, can introduce large errors in the calculation of G_s'' and G_s' , in coincidence with other interfacial rheometers, such as the DWR [8] and the ISR [6, 9].

Finally, we have tested our ensemble by performing measurements on well known fatty acid monolayers and comparing the results obtained against measurements made by means of a high resolution magnetic tweezers ISR [12]. The measurements were made on the L2 phase of the C24 and the L2 and LS phases of the C15 fatty acid monolayers. Both rheometers yield nicely superposing results within the limits that are measurable with the rotational rheometer with the conical bob fixture ensemble using the data processing here proposed, and taking into account the resolution here estimated.

SUPPLEMENTARY MATERIAL

See supplementary material for the experimental determination of the conical bob + rotor moment of inertia, details on the zero thickness disk approximation, a discussion on the frictional torque appearing at the air bearing rotor of the rheometer, and more $f - \arg(Bo^*)$ combinations for Figs. 5, 7, and 8.

ACKNOWLEDGMENTS

J.T. acknowledges a grant from UNEDs Researchers Formation Program. M.A.R. and J.M.P. acknowledge partial support from MINECO (Grant No. FIS2013-47350-C5-5-R), and J.M.P. from MINECO (Grant No. MTM2015-63914-P). The authors also acknowledge Francisco Ortega, Ramón G. Rubio and Eduardo Guzmán for fruitful discussions.

---

[1] D. Langevin, "Influence of interfacial rheology on foam and emulsion properties," Advances in Colloid and Interface Science **88**, 209–222 (2000).

[2] P. J. Wilde, "Interfaces: Their role in foam and emulsion behaviour," Current Opinion in Colloid and Interface Science **5**, 176–181 (2000).

[3] Fo Opawale and Dj Burgess, "Influence of interfacial properties of lipophilic surfactants on water-in-oil emulsion stability," Journal of colloid and interface science **197**, 142–50 (1998).

[4] D. T. Wasan, J. J. McNamara, S. M. Shah, K. Sampath, and N. Aderangi, "The role of coalescence phenomena and interfacial rheological properties in enhanced oil recovery: An overview," Journal of Rheology **23** (1979).

[5] Huan-Quan Sun, Lei Zhang, Zhen-Quan Li, Lu Zhang, Lan Luo, and Sui Zhao, "Interfacial dilational rheology related to enhance oil recovery," Soft Matter **7**, 7601–7611 (2011).

[6] Sven Reynaert, Carlton F. Brooks, Paula Moldenaers, Jan Vermant, and Gerald G. Fuller, "Analysis of the magnetic rod interfacial stress rheometer," J. Rheol. **52**, 261 (2008).

[7] LE Scriven, "Dynamics of a fluid interface equation of motion for newtonian surface fluids," Chem. Eng. Sci. **12**, 98–108 (1960).

[8] Steven Vandebril, Aly Franck, Gerald G. Fuller, Paula Moldenaers, and Jan Vermant, "A double wall-ring geometry for interfacial shear rheometry," Rheologica Acta **49**, 131–144 (2010).

[9] Tom Verwijlen, Paula Moldenaers, Howard A Stone, and Jan Vermant, "Study of the flow field in the magnetic rod interfacial stress rheometer," Langmuir **27**, 9345–9358 (2011).

[10] Philipp Erni, Peter Fischer, Erich J Windhab, Victor Kusnezov, Heiko Stettin, and Jörg Läuger, "Stress-and strain-controlled measurements of interfacial shear viscosity and viscoelasticity at liquid/liquid and gas/liquid interfaces," Rev. Sci. Instrum. **74**, 4916–4924 (2003).

[11] D Rossetti, GE Yakubov, JR Stokes, A-M Williamson, and GG Fuller, "Interaction of human whole saliva and astringent dietary compounds investigated by interfacial shear rheology," Food Hydrocolloids **22**, 1068–1078 (2008).

[12] J. Tajuelo, J. M. Pastor, and M. A. Rubio, "A magnetic rod interfacial shear rheometer driven by a mobile magnetic trap," J. Rheol. **60** (2016).

[13] Zachary A. Zell, Vincent Mansard, Jeremy Wright, KyuHan Kim, Siyoung Q. Choi, and Todd M. Squires, "Linear and nonlinear microrheometry of small samples and interfaces using microfabricated probes," J. Rheol. **60** (2016).

[14] DY Zang, E Rio, D Langevin, B Wei, and BP Binks, "Viscoelastic properties of silica nanoparticle monolayers at the air-water interface," Eur. Phys. J. E **31**, 125–134 (2010).

[15] Jin-Mi Jung, Deniz Zeynel Gunes, and Raffaele Mezzenga, "Interfacial activity and interfacial shear rheology of native β-lactoglobulin monomers and their heat-induced fibers," Langmuir **26**, 15366–15375 (2010).

[16] Armando Maestro, Laura J. Bonales, Hernan Ritacco, Thomas M. Fischer, Ramón G. Rubio, and Francisco Ortega, "Surface rheology: macro- and microrheology of poly(tert-butyl acrylate) monolayers," Soft Matter **7**, 7761 (2011).

[17] Soo Gun Oh and John C Slattery, "Disk and biconical interfacial viscometers," J. Colloid Interface Sci. **67**, 516–525 (1978).

[18] Yia-Ching Ray, Hae Ok Lee, Tsung Leo Jiang, and Tsung-Shann Jiang, "Oscillatory torsional interfacial viscometer," J. Colloid Interface Sci. **119**, 81–99 (1987).

[19] J Tajuelo, J M Pastor, F Martínez-Pedrero, M Vázquez, F Ortega, R. G. Rubio, and M A Rubio, "Magnetic microwire probes for the magnetic rod interfacial stress rheometer," Langmuir **31**, 1410–1420 (2015).

[20] Vladimir M Kaganer, Helmuth Möhwald, and Pulak Dutta, "Structure and phase transitions in langmuir monolayers," Rev. Mod. Phys. **71**, 779–819 (1999).

[21] Juan M Lopez and Amir H Hirsa, "Coupling of the interfacial and bulk flow in knife-edge viscometers," Phys. Fluids **27**, 042102 (2015).

[22] Sean Fitzgibbon, Eric S. G. Shaqfeh, Gerald G. Fuller, and Travis W. Walker, "Scaling analysis and mathematical theory of the interfacial stress rheometer," J. Rheol. **58** (2014).

[23] R Nagarajan, SI Chung, and DT Wasan, "Biconical bob oscillatory interfacial rheometer," J. Colloid Interface Sci. **204**, 53–60 (1998).

[24] Christophe Baravian, Ghania Benbelkacem, and François Caton, "Unsteady rheometry: can we characterize weak gels with a controlled stress rheometer?" Rheologica Acta **46**, 577–581 (2007).

[25] Carlton F Brooks, Gerald G Fuller, Curtis W Frank, and Channing R Robertson, "An interfacial stress rheometer to study rheological transitions in monolayers at the air - water interface," Langmuir **5**, 2450–2459 (1999).

[26] Coralie Alonso and Joseph A Zasadzinski, "A brief review of the relationships between monolayer viscosity, phase behavior, surface pressure, and temperature using a simple monolayer viscometer," J. Phys. Chem. B **110**, 22185–22191 (2006).

[27] AM Bibo, CM Knobler, and IR Peterson, "A monolayer phase miscibility comparison of long-chain fatty acids and their ethyl esters," J. Phys. Chem. **95**, 5591–5599 (1991).

[28] T. Verwijlen, L. Imperiali, and J. Vermant, "Separating viscoelastic and compressibility contributions in pressure-area isotherm measurements," Adv. Colloid Interface Sci. **206**, 428 – 436 (2014).

[29] Laura J Bonales, Hernán Ritacco, José E F Rubio, Ramón G Rubio, and F Monroy, "Dynamics in ultrathin films : Particle tracking microrheology of lang- muir monolayers," The Open Physical Chemistry Journal , 25–32 (2007).